Check for updates

Recent advances of metal active sites in photocatalytic CO₂ reduction

Wa Gao, [ID] *[a] Haonan Li,[a] Jianqiang Hu, [ID] [f] Yong Yang,*[e] Yujie Xiong, [ID] [h] Jinhua Ye,[g] Zhigang Zou[cd] and Yong Zhou [ID] *[bcd]

Photocatalytic CO₂ reduction captures solar energy to convert CO₂ into hydrocarbon fuels, thus shifting the dependence on rapidly depleting fossil fuels. Among the various proposed photocatalysts, systems containing metal active sites (MASs) possess obvious advantages, such as effective photogenerated carrier separation, suitable adsorption and activation of intermediates, and achievable C–C coupling to generate multi-carbon (C₂₊) products. The present review aims to summarize the typical photocatalytic materials with MAS, highlighting the critical role of different formulations of MAS in CO₂ photoreduction, especially for C₂₊ product generation. State-of-the-art progress in the characterization and theoretical calculations for MAS-containing photocatalysts is also emphasized. Finally, the challenges and prospects of catalytic systems involving MAS for solar-driven CO₂ conversion are outlined, providing inspiration for the future design of materials for efficient photocatalytic energy conversion.

1 Introduction

Over-reliance on fossil fuels as energy carriers leads to excessive CO₂ emissions from combustion, which in turn causes climate change, environmental damage and energy crisis.[1–3] Shifting from fossil fuels to renewable energy sources to achieve carbon neutrality is an important step towards sustainable development. Therefore, there is an urgent need to find a suitable, effective, and green strategy to facilitate the conversion of CO₂ and access renewable energy through sustained technological innovation.

CO₂ capture and conversion by artificial photosynthesis can simultaneously address the rising global CO₂ emissions and produce hydrocarbon fuels to accomplish carbon neutrality.[4–6]

It is proving to be an elegant and promising solution, attracting the interest of scientists and making great strides in the efficiency of CO₂ conversion.[7–11] Specifically, the photocatalytic reduction of CO₂ achieves a sustainable alternative to conventional fossil fuels, which is carried out in relatively mild conditions-room temperature and pressure, driving the conversion of CO₂ to hydrocarbons directly without additional energy supply or harmful substance release. Photocatalytic CO₂ reduction consists of three main processes:[12] the catalyst generates electron–hole pairs under sunlight;[13–15] carriers separate and migrate to the surface;[16] CO₂ is activated and converted at the surface active sites, involving C–O bond breaking, C–H bond formation, and C–C coupling.[17,18] In fact, the CO₂ molecule possesses a rather stable structure with high dissociation energy to cleave the C=O bond (750 kJ mol⁻¹), which poses a challenge for the activation and conversion of CO₂.[19] In addition, solar-driven CO₂ reduction involves complex multi-step conversions that, depending on the number of electrons and protons transferred, produces CO,[20–22] CH₃OH,[23–25] CH₄,[26,27] C₂H₄,[28–30] C₂H₆,[31,32] C₂H₅OH,[33] *etc.* Due to the diversity of products of CO₂ photoreduction, achieving highly selective CO₂ conversion to generate specific target products is extremely challenging.

Various strategies have been employed to improve the efficiency and selectivity of CO₂ photoreduction, including enhancing light absorption,[34,35] promoting carrier separation,[36] constructing active sites,[37] and promoting C–C coupling.[38] According to the current findings, MAS possesses significant advantages in improving the performance of photocatalytic reduction of CO₂ and promoting C–C coupling to obtain C₂₊ products.[39–41] This review mainly introduces the research

[a]School of Physical Science and Technology, Tiangong University, Tianjin 300387, P. R. China

[b]School of Chemical and Environmental Engineering, Anhui Polytechnic University, Wuhu 241000, P. R. China

[c]School of Physics, Jiangsu Key Laboratory of Nanotechnology, Eco-materials and Renewable Energy Research Center (ERERC), National Laboratory of Solid State Microstructures, Collaborative Innovation Center of Advanced Microstructures, Nanjing University, Nanjing 210093, P. R. China

[d]School of Science and Engineering, The Chinese University of Hongkong (Shenzhen), Shenzhen, Guangdong 518172, P. R. China

[e]Key Laboratory of Soft Chemistry and Functional Materials (MOE), Nanjing University of Science and Technology, Nanjing 210094, P. R. China

[f]Jiangxi Normal Univ., Inst. Adv. Mat. IAM, Coll. Chem. & Chem. Engn., Nanchang 330022, P. R. China

[g]National Institute for Materials Science (NIMS), International Center Materials Nanoarchitecture MANA, 1-1 Namiki, Tsukuba, Ibaraki 305-0044, Japan

[h]School of Chemistry and Materials Science, University of Science and Technology of China, Hefei 230036, Anhui, P. R. China

progress of MAS in driving photocatalytic CO_2 conversion (Fig. 1). Photocatalytic systems containing MAS including metal oxides, metal sulfides, layered double hydroxides (LDHs), metal organic framework (MOF), covalent organic frameworks (COF), single atom catalysts, and metal complexes are summarized. The achievement of MAS with different formulations in photocatalytic CO_2 conversion is systemically explored while mechanisms that drive performance improvement are discussed in detail. The development of characterization techniques and theoretical calculation to determine the structure and function of MAS in CO_2 photoreduction is also highlighted. Finally, the difficulties, challenges, and novel viewpoints of feasible solutions are addressed regarding the design of advanced photocatalysts containing MAS for efficient solar energy conversion.

2 Photocatalytic systems with MAS

Micro-nanostructures containing MAS, including metal oxides, metal sulfides, LDHs, MOF, COF, single atom catalysts, and metal complexes are widely used in photocatalytic CO_2 reduction. According to the process and mechanism of CO_2 photoreduction, the catalytic systems with high light absorption capacity, sufficient carrier separation, and abundant active sites show obvious advantages in the yield and selectivity of CO_2 conversion.

2.1 Metal oxides

In the complex and diverse photocatalytic systems, metal oxides have become the most representative and well-established photocatalysts. A large number of strategies aimed at modulating the band gap, facilitating carrier separation, and establishing active sites have been proposed and intensively investigated in metal oxides.[42–44] TiO_2, as a representative metal oxide, has become a photocatalyst of wide interest due to its low toxicity, high stability and economic advantages. Defect engineering, heterostructure construction, heteroatom doping, and surface modulation have been proposed to regulate the carrier

migration, CO_2 adsorption and activation of TiO_2-based catalysts. The synergistic effect of Ru and oxygen vacancies (Vo) on the photocatalytic performance of TiO_2 (Ru–TiO_{2-x}) was systematically investigated.[45] It was found that Ru–TiO_{2-x} exhibited high activity for the photoreduction of CO_2 to CH_4. The introduced Vo in Ru–TiO_{2-x} provided important contributions to promote photogenerated carrier separation and facilitate CO_2 conversion. The Ru species effectively captured photogenerated electrons, which inhibited further photogenerated carrier recombination.

Photocatalytic CO_2 reduction for the generation of C_{2+} products was achieved in metal–oxide systems. The vacancy-rich TiO_2 with Cu single atoms loading produced C_3H_8, which involved an overall 20 e^- reduction and two sequential C–C coupling processes.[46] The Cu–Ti–V_O unit in the $Ti_{0.91}O_2$ matrix was formed through the modulation of the electronic coupling interaction between the Cu atoms and adjacent Ti atoms by Vo. This unique unit lowered the energy levels of the key *CHOCO and *CH_2OCOCO intermediates, thereby tuning the C_1–C_1 and C_1–C_2 couplings to thermodynamically favourable exothermic processes (Fig. 2a). Moreover, the metastable hexagonal WO_3 (h-WO_3), offering a suitable bandgap, exhibited efficient photoreduction of CO_2 to C_2H_4.[47] The blue color of the metastable state of WO_3 was attributed to the reduction of W^{6+} to W^{5+} or W^{4+} with the increase of the reduced state, which indicated the existence of Vo. The surface Vo enhanced the light absorption capability and promoted the photogenerated carrier separation. More importantly, the W–S–W sites formed by the S atom,
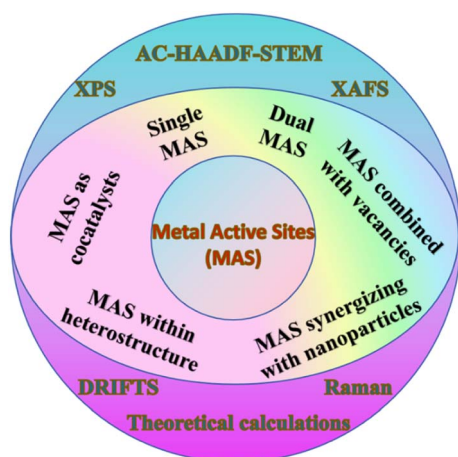

Fig. 1 Overview of the metal active sites in photocatalytic CO_2 reductions.
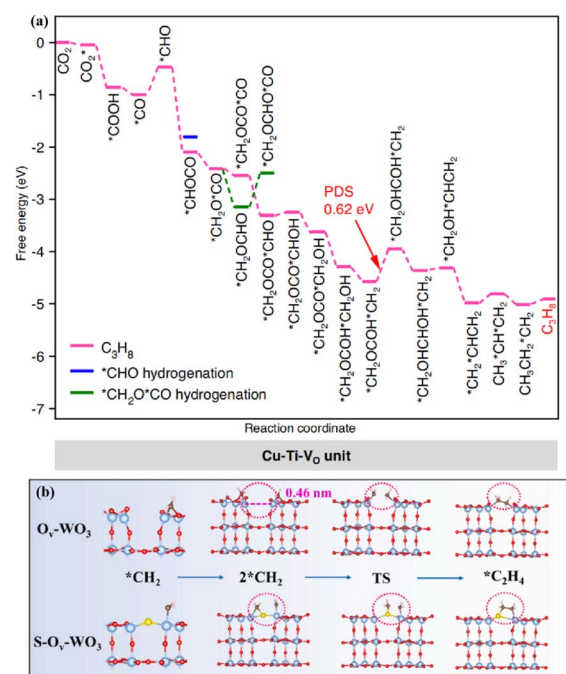

Fig. 2 (a) Gibbs free energy diagrams of CO_2 reduction on the Cu–Ti–V_O unit. This figure has been reproduced from ref. 46 with permission from Springer Nature, copyright 2023. (b) The C–C coupling process of Ov–WO_3 and S–Ov–WO_3. This figure has been reproduced from ref. 47 with permission from Elsevier, copyright 2023.

which replaced oxygen atoms and bridged the adjacent W atoms, benefited the adsorption of *CH₂ intermediates and promoted the C–C coupling to generate C_2H_4 (Fig. 2b).

Based on the above analysis, the MAS constructed in the metal oxide system is structurally stable, successfully achieving efficient photocatalytic CO_2 conversion with C_{2+} generation. In fact, MAS in metal oxides often synergizes with defect and doping atoms to achieve performance enhancement. Therefore, MAS introduced in metal oxides usually needs multi-step experimental treatment processes.

2.2 Transition metal sulfides/phosphorus sulfides

Various metal chalcogenides, such as ZnS, CdS, MnS, CdSe, $ZnIn_2S_4$ (ZIS), and $CuIn_5S_8$, have exhibited progressive photocatalytic performances. Their excellent properties, including their low cost, wide range of light absorption, and high carrier mobility, have made them one of the most promising materials for CO_2 conversion.

The reduction potential of ZnS is -1.04 V *vs.* NHE, which is relatively negative and particularly suitable for the photocatalytic reduction reaction.[48] However, the wide band gap (3.6–3.8 eV), fast recombination of the charge carriers, and low selectivity toward CO_2 reduction competing with the hydrogen evolution reaction (HER) limit the efficiency of ZnS. Cu-doped ZnS, containing abundant sphalerite and wurtzite phase (S–W) junctions, enhanced the photocatalytic activity with high CO selectivity.[49] The S–W phase junction containing abundant sulfur vacancies (Vs) effectively facilitated the separation of charge carriers and the localization of photoelectrons for surface catalysis. The addition of Cu increased the electron density at the Fermi energy level, promoted the reactivity of the Cu sites, and enhanced the bonding of the catalyst surface to the *CO intermediate, thereby improving the CO selectivity. Furthermore, the dual functional ZnS coupled with g-C₃N₄ simultaneously enhanced the surface and bulk carrier separation of g-C₃N₄ for the highly selective reduction of CO_2 to CH_4.[50] ZnS acted as a cocatalyst to capture the photogenerated electrons of g-C₃N₄. It contributed a polarization electric field, which was created inside the ZnS nanoparticle along the direction of spontaneous polarization, to prompt the migration and separation of photogenerated charges from bulk to surface.

ZIS, belonging to the AB_2X_4 group of ternary compounds, has been used in photocatalysis with visible light absorption.[53] The metallic $ZnIn_2S_4$, which is rich in indium vacancies (V_{In}), exhibited full-spectrum responsiveness for high CO_2 photoreduction efficiency.[51] The V_{In} defect state captured the excited hole (h^+) and increased the minority carrier diffusion length, resulting in a large number of carriers moving to the surface and participating in the conversion of CO_2. Theoretical calculations revealed that V_{In} lowered the energy barrier of the rate-limiting step (the formation of COOH*, Fig. 3a and b), leading to the high rate of CO evolution. In addition, anchoring single Au atoms to ultrathin ZIS (Au₁/ZIS) nanosheets with Vs resulted in the Au_1–S_2 low coordination structure, which enabled exceptional photocatalytic CO_2-to-CH_4 conversion.[52] The introduction of Au single atoms enhanced the efficiency of carrier
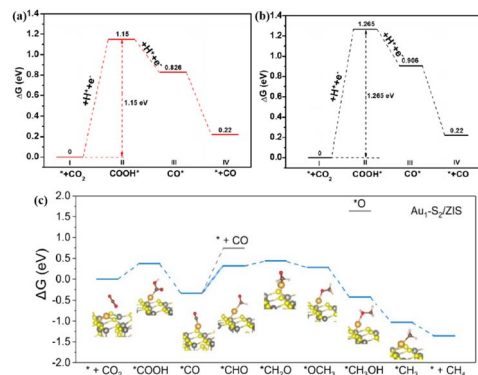

Fig. 3 Free energy diagrams for the reduction of CO_2 to CO over the (001) facets of V_{In}-rich-ZIS (a) and V_{In}-poor-ZIS (b). These figures have been reproduced from ref. 51 with permission from American Chemical Society, copyright 2022. Free energy diagrams of photocatalytic CO_2 to CH_4 for Au_1–S_2/ZIS (c). This figure has been reproduced from ref. 52 with permission from Wiley-VCH, copyright 2022.

separation and transfer. Moreover, the low-coordinated single Au atom significantly enhanced CO_2 activation, lowered the energy barrier for *CO protonation, and stabilized the *CH₃ intermediate, leading to the selective generation of CH_4 by CO_2 photoreduction.

Transition metal phosphorous trichalcogenides have been well-explored in the photoreduction of CO_2 to valuable fuels. The introduction of Vs in $AgInP_2S_6$ regulated the CO_2 photoreduction reaction pathway to steer the dominant generation of C_2H_4.[54] The V_S led the charge accumulation on the Ag atoms near V_S, which effectively captured the forming *CO. This phenomenon enriched the catalyst surface with key reaction intermediates and promoted C–C coupling to generate C_2 species with low binding energy barriers. In addition, the tandem synergistic effect of the charge-enriched Cu–In dual site, which was confined on the lateral edge of the $CuInP_2S_6$ monolayer, became the main reason for the efficient conversion and high selectivity of C_2H_4.[55] In the presence of light, the limbic In site of the $CuInP_2S_6$ monolayer converted CO_2 mainly to *CO, which was transferred to the neighbouring Cu site for the subsequent C–C coupling reaction to C_2H_4.

By reason of the foregoing, MAS in metal chalcogenides shows unique advantages in the generation of C_{2+} products. However, due to the limitation of the stability of the metal sulfide, the stability of MAS in them may be lacking. Therefore, in photocatalytic applications, attention should be paid to improving the stability of MAS in metal sulfides.

2.3 LDHs

LDHs are typically layered materials consisting of laminates and interlaminar anions with a high degree of flexible tunability in terms of morphology and ionic composition.[57] The adjustment of the metal cation or anion in LDH can easily regulate the electronic structure and influence the CO_2 conversion process. For example, the selectivity of the photocatalytic reaction could be precisely tuned by the composition of metal cations in the ZnM-LDH photocatalysts (M = Ti^{4+}, Fe^{3+}, Co^{3+}, Ga^{3+}, Al^{3+}).[56]

Specifically, the main reduction product of ZnTi-LDH was CH_4. ZnFe-LDH and ZnCo-LDH generated H_2 by water splitting, and ZnGa-LDH and ZnAl-LDH produced CO (Fig. 4a and b). Experimental characterization and theoretical calculations revealed that the d-band center of the M^{3+} or M^{4+} cations affected the adsorption strength of CO_2: cations with the d-band centers close to the Fermi level adsorbed CO_2 strongly, benefiting CH_4 or CO formation. Conversely, the deviation of the d-band centre from the Fermi level led to poor CO_2 adsorption and hence H_2 production. In addition, the strategies involving morphology modulation, heterostructure construction, doping, and defect introduction have a crucial effect on the CO_2 conversion process of LDH. The S-scheme heterojunction of g-C_3N_4/CoCo-LDH preserved the water oxidation ability of CoCo-LDH and redox ability of g-C_3N_4.[58] The atomic-level interface chemical bond (Co–N_2 bond) of g-C_3N_4/CoCo-LDH realized the high-speed transfer of electrons. The addition of CoCo-LDH benefited the CO_2 adsorption, reduced the energy barrier of the key intermediate *COOH, and promoted water decomposition.

Obviously, MAS can take advantage of the two-dimensional (2D) structure, as well as the highly flexible adjustability in the morphology and ionic composition of LDH. However, the synergies of different metals and their roles in C_{2+} generation remain to be explored.

2.4 MOF

One of the crystalline porous materials, MOF, which possesses diversified metal ions/clusters and organic linkers, as well as atomically precise and tailorable structures, provides the natural MAS for catalysis.[60] Zirconium-based MOF (PCN-222) hybridized with cellulose acetate (CA@PCN-222) increased the activity of CO_2 photoreduction to formate compared with pristine PCN-222 by regulating the atomic interface structure of the MAS (Fig. 5a).[59] The valence band (VB) across the Fermi energy levels resulted in higher charge-transfer kinetics of CA@PCN-222 relative to PCN-222. The interfacial electron transfer from
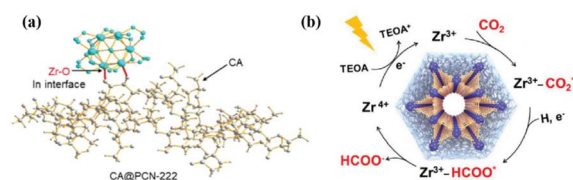

Fig. 5 (a) Schematic atomic interface model of CA@PCN-222. (b) Proposed mechanism for the CO_2 photoreduction reaction over CA@PCN-222. These figures have been reproduced from ref. 59 with permission from Wiley-VCH, copyright 2023.

CA to PCN-222 led to the redistribution of the Zr d-orbital electrons. Moreover, the Zr^{IV}-cluster unit in CA@PCN-222 was turned into a Zr^{III}-cluster active site after accepting two electrons from two adjacent tetrakis(4-carboxyphenyl)-porphyrin ligands under visible-light irradiation, which selectively reduced CO_2 to $HCOO^-$ in a two-electron process (Fig. 5b).

The modulation of the coordination environment around the MAS in MOFs helps to reveal the relationship between structure and activity during CO_2 photoreduction. In UiO-type MOFs bearing bipyridine linkers, the number of coordinated N atoms around a single Co site was tuned to provide UiO-Co-N_x (x = 2, 3 and 4) for photocatalytic CO_2 reduction.[61] UiO-Co-N_3 exhibited superior activity to the other counterparts, which was mainly attributable to the difference in the number of coordinating N atoms around the Co site. Particularly, UiO-Co-N_3 endowed the lowest energy barriers of the rate-determining step ($CO_2 \rightarrow COOH^*$) and the desorption of CO* among all UiO-Co-N_x samples, accounting for the optimized CO_2 photoreduction activity.

The MAS in MOF enables liquid C_{2+} generation. The specific NH_2–Cu–NH_2 triple atom site was constructed by incorporating Cu sites into the connected nodes of defective UiO-66-NH_2, realizing photocatalytic CO_2-to-acetone conversion.[62] Specifically, one of the N active sites on the NH_2–Cu–NH_2 adsorbed CO_2 and converted CO_2 to form *CH_3 ($CO_2 \rightarrow COOH^* \rightarrow CO^* \rightarrow$ *CH_3). Meanwhile, the Cu site activated its adsorbed CO_2 to CO*. *CH_3 and *CO underwent the first C–C coupling on CuN_2O_2 to generate *CO–*CH_3. At the same time, another N site on the CuN_2O_2 fragment activated the adsorbed CO_2 into CO*, which underwent a second C–C coupling process with the *$COCH_3$ intermediate to generate the crucial *$COCOCH_3$. Due to the synergistic interaction between the Cu site and the N site, the C_2 intermediate on the CuN_2O_2 ultimately generated C_3.

In summary, the MAS in MOF connected with organic ligands exhibits good dispersion and high utilization, which can make full use of the porous property of MOF to optimize the photocatalytic CO_2 reduction performance. However, its synthesis process involves complex chemical reactions and utilizes expensive organic ligands, making practical production applications difficult.

2.5 COF

COF is a class of organic polymers linked by reversible covalent bonds, which possesses periodical structures, well-defined porosity, an extended π-conjugated framework, and pore
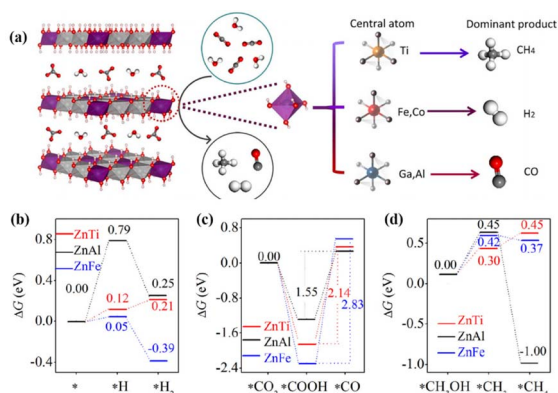
Fig. 4 (a) Scheme showing CO_2 and H_2O photoreduction on the different ZnM-LDH photocatalyst (carbon: dark gray; oxygen: red; hydrogen: white). DFT calculations of the elementary steps of (b) H_2 evolution, (c) CO_2 reduction to CO, and (d) CO_2 reduction to CH_4 involving a methanol intermediate over ZnTi-LDH, ZnAl-LDH, and ZnFe-LDH. These figures have been reproduced from ref. 56 with permission from Elsevier, copyright 2020.

structures for mass transfer. An adequate MAS of COF could be constructed by incorporating metal atoms into the skeletons or pore channels by coordination interaction.[63] 2D COF ultrathin nanobelts coordinated with single Cu–O/N sites (Cu^{2+} anchored by both O and N) exhibited high CO selectivity of 94% under visible-light-driven CO_2 reduction.[64] Crucially, the Cu–O/N sites benefited the electron transfer from COF upon light irradiation, and served as the active sites for the highly selective reduction of CO_2 to CO. Two types of cobalt Schiff base COF composites, Co-2,3-DHTA-COF with Co–O_4 sites and Co-TP-COF with Co-O_3N sites, realized the CO_2 photoreduction into CO (Fig. 6).[65] The supereminent photocatalytic performance of Co-COF with Co-O_4 sites was mainly attributed to the high CO_2 adsorption capacity, low charge-transfer resistance, strong separation of electrons and holes, and the lower energy barrier in the ligand exchange process between Co-2,3-DHTA-COF and CO_2. For hydrocarbon product generation, single-atom MoN_2 sites were introduced into COF (Mo-COF) to realize the photoreduction of CO_2 to CH_4 and C_2H_4 under visible light.[66] The MoN_2 sites contributed to the efficient separation efficiency of photo-generated electrons and holes, enhanced the adsorption and activation of CO_2 and CO, and reduced the energy barriers for the formation of hydrocarbon intermediates, thus leading to the production of high value-added hydrocarbons over Mo-COF.

Particularly, MAS can utilize the π-conjugated framework in COF to promote the photogenerated carrier separation and enhance the photocatalytic CO_2 reduction. However, MAS needs to be grafted onto the COF structure with fine regulation. In addition, the construction of multiple MAS in COF and the study of their catalytic mechanism still need to be continuously explored.

2.6 Single-atom catalysts

Single-atom catalysis with MAS uniformly and individually loaded on a supporting material provides a research platform for structure–performance correlation at the atomic level. Atomically dispersed MAS improves the atomic utilization, modulates the charge distribution of the catalyst, and affects the adsorption and conversion of reactants and intermediates, ultimately influencing the product efficiency and selectivity of the photocatalytic CO_2 reduction.
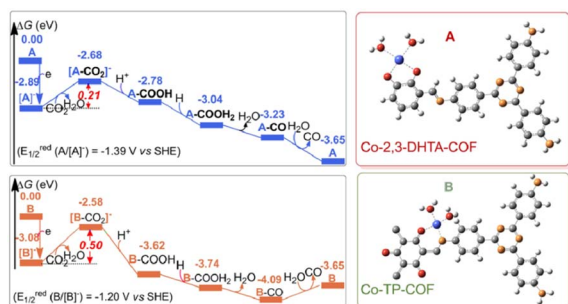
Loading rare-earth La single atoms on carbon nitride (O/La–CN) constructed the active centers of La–N charge-transfer bridges for photocatalytic CO_2 reduction.[67] Electronic state changes induced by the hybridization of the 4f and 5d orbitals of La single atoms and the p–d orbitals of La–N atoms established charge-transfer channels for La–N bridges to promote carrier separation. Bader charge and differential charge distributions suggested that electrons were transferred through La atoms into connected N atoms, and eventually through C atoms to O atoms. The O/La–CN strengthened CO_2 adsorption, endowed the high capacity for CO_2 uptake, and reduced the activation energy barrier for COOH* formation. Moreover, the desorption of CO from the surface of O/La–CN required the lowest energy (0.2 eV) compared with the dissociation reaction (COH*, 2.96 eV and C* + H_2O, 4.59 eV) or hydrogenation (HCO*, 1.53 eV), contributing CO formation with high selectivity (Fig. 7a). Cu loading on BiOBr nanosheets (Cu_1@BiOBr) established a strong built-in electric field with isolated Cu sites that acted as electron traps to promote charge transfer and stabilize charge carriers.[68] The high selectivity of methanol within this photocatalytic system could be ascribed to the energy-favorable hydrogenation of the *CO intermediate into *CHO (Fig. 7b). Furthermore, the unfavorable adsorption of CH_3OH on Cu_1@-BiOBr relative to H_2O prevented methanol from being oxidized by photogenerated holes.

In addition to single MAS loading, dual MAS incorporation has been explored to drive CO_2 photoreduction with diverse functions. The dual MAS of cobalt (Co) and ruthenium (Ru) supported on a conjugated porous carbon nitride polymer exhibited efficient photocatalytic CO_2 reduction.[69] *In situ* characterizations and theoretical calculations revealed that the active Co sites facilitated dynamic charge transfer, along with Ru working as adsorption sites for CO_2 photoactivation. In detail, the atomic Co facilitated dynamic electron transfer from

Fig. 6 Gibbs energy profiles of the CO_2RR-to-CO reaction over Co-2,3-DHTA-COF (A, blue line) and Co-TP-COF (B, orange line). This figure has been reproduced from ref. 65 with permission from American Chemical Society, copyright 2023.
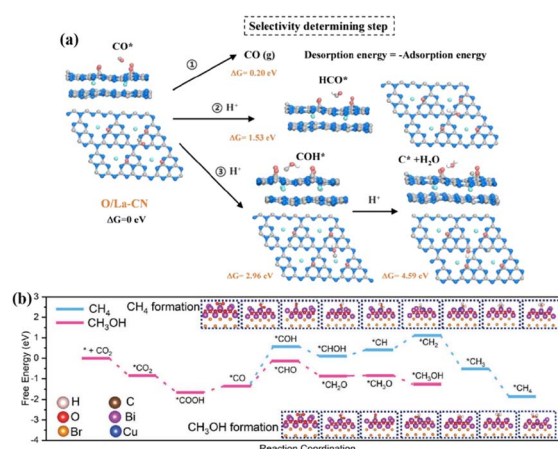
Fig. 7 (a) Calculated free energy for the photocatalytic CO_2 reduction reaction of the selectivity-determining step. This figure has been reproduced from ref. 67 with permission from American Chemical Society, copyright 2020. (b) The DFT-calculated free energy diagram for the hydrogenation of CO_2 to CH_3OH and CH_4 over Cu_1@BiOBr. This figure has been reproduced from ref. 68 with permission from Wiley-VCH, copyright 2023.

the carbon nitride polymer to the atomic Ru site, resulting in the COOH* intermediate being effectively stabilized by the charged-rich Ru site. Moreover, the smaller Gibbs free energy of CO formation than that of the protonation of CO* to CHO* resulted in high CO selectivity. Similarly, Ru and Cu single atoms simultaneously incorporated into polymeric carbon nitride (poly-CN) exhibited higher selectivity (95%) for CH_4 production than that decorated with Ru or Cu individually.[70] The atomically dispersed $Ru-N_4$ and $Cu-N_3$ sites tuned the electronic structure of poly-CN, and were identified as active centers. During CO_2 photoreduction, the Ru single atom was essential for proton production, while the Cu single atom played a dominant role in the reduction process. Due to the thermodynamically more favorable conversion of *CO to *CHO, the coexistence of the Ru and Cu single atoms resulted in the efficient conversion of CO_2 to CH_4.

Remarkably, the MAS in single-atom catalysts exhibits high metal atom utilization and achieves synergistic effects of multiple MASs. However, the metal is easily aggregated to form particles during the construction process. Thus, a delicate experimental design is required to successfully construct MAS in single-atom form.

2.7 Metal complexes

The realization of CO_2 photoreduction by transition metal complexes with tunable and definable chemical structures is accompanied by the activation and immobilisation of neutral CO_2 molecules at the metal centre.[71] By installing a 2-phenol, 2-amino or 2-mercapto to a tripodal skeleton, the Co-based homogeneous catalysts (named $[CoN_3O]ClO_4$, $[CoN_4]ClO_4$ and $[CoN_3S]ClO_4$, respectively) possessed different coordination microenvironments for CO_2 reduction.[72] The optimal $[CoN_3O]$ ClO_4 photocatalyst had a maximum turnover number (TON) of 5652 in photocatalytic CO_2 reduction among $[CoN_4]ClO_4$ and $[CoN_3S]ClO_4$. The strong electronegativity of the oxygen atom in the ligand endowed the Co(II) catalytic center with a low reduction potential and more stable *COOH intermediate, thus substantially promoting the CO_2-to-CO conversion. The dinuclear heterometallic $[CuNiL^2]$ showed the highest CO_2-to-CO conversion relative to dinuclear homometallic $[Ni_2L^2(CH_3\text{-}OH)_2]$ and mononuclear $[NiL^1(CH_3OH)]$.[73] A theoretical calculation revealed that the introduction of inactive Cu^{II} in CuNi-L^2 promoted the transportation of photo-generated electrons to the coupled active Ni^{II} site. This allowed Ni^{II} with an O_4 coordination environment in $[CuNiL^2]$ to express strong reducing ability, which significantly accelerated the photocatalytic CO_2-to-CO conversion.

Metal complexes could drive C–C coupling to generate C_{2+} products. The synergistic dual sites of rhenium(I) bipyridine fac-$[ReI(bpy)(CO)_3Cl]$ (Re-bpy) and copper porphyrinic triazine framework [PTF(Cu)] working in tandem strategy achieved the photocatalytic conversion of CO_2 to C_2H_4 (Fig. 8).[74] The CO generated at the Re-bpy sites was adsorbed by the nearby Cu single sites in PTF(Cu), followed by a synergistic C–C coupling process to ultimately produce C_2H_4. Critically, Rebpy-*CO could enter the porous PTF(Cu) and move to the nearby Cu–*CO,
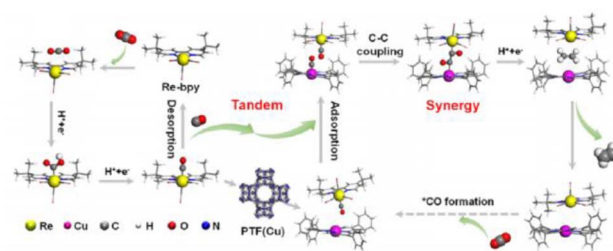

Fig. 8 Tandem catalysis mechanism of Re-bpy/PTF(Cu). This figure has been reproduced from ref. 74 with permission from American Chemical Society, copyright 2023.

leading to practicable free energy for the CO–CO coupling between Cu–*CO and Re-bpy-*CO (Re-bpy-*CO-*CO-PTF(Cu)). However, PTF(Cu) catalysts alone produced CO under similar conditions. This was caused by the large distance between the adjacent Cu centers in PTF(Cu) hindering C_{2+} formation via the coupling of Cu–*CO–*CO–Cu.

As mentioned above, the alteration of the MAS coordination environment can be achieved by modulating the skeleton in metal complexes, which in turn regulates the photocatalytic CO_2 reduction performance. It is conducive to revealing the in-depth reaction mechanism. However, the typical problems in photocatalysis, such as the high separation cost and low chemical stability, still limit their practical applications.[75]

3 Different formulations of MAS in the photocatalytic CO_2 reduction

Incorporation of MAS can regulate the transport of photo-generated carriers, increase the local electron density of the adsorption sites, affect the adsorption strength of reactants and intermediates, and ultimately adjust the barrier and selectivity of the reaction. In this section, the role of different formulations of MAS in photocatalytic CO_2 reduction is described in detail (Table 1).

3.1 Single MAS

The incorporation of individual MAS into the catalyst backbone from an atomic level perspective maximizes atomic utilisation efficiency and optimizes the performance of photocatalytic CO_2 conversion. The bipyridine-based polyimide polymer (Bpy-PDI) anchoring single Ni site achieved diluted CO_2 photoreduction with high generation activity for CO_2-to-CO in 0.1 atm CO_2 pressure.[76] The obviously larger adsorption energy of CO_2 for the Ni site (1.44 eV) compared to that of Bpy-PDI (0.19 eV) indicated a much stronger adsorption affinity of the Ni site towards CO_2. Moreover, the free energy of COOH* generation (the rate-determining step) on the Ni sites (−0.07 eV) was obviously smaller than that of Bpy-PDI (1.69 eV), revealing the contribution of the dispersed Ni atom toward the energy barrier decline. Cu single atoms on the nitrogen-doped carbon anchored on TiO_2 with the anatase–rutile mixed phase exhibited 100% CO selectivity in the photocatalytic CO_2 reduction.[77] Cu single atoms became the adsorption and activation sites for

Table 1 Different formulations of MAS in photocatalytic CO_2 reduction

	Catalyst	Reactive sites	Light source	Reaction condition	Performance (μmol g^{-1} h^{-1})	Ref.
Single MAS	Cu-doped ZnS containing abundant S-W junctions	Cu	300 W Xe lamp	18 mL solution containing chloroform + 2 mL 2-propanol + CO_2	CO: 68.9 (99.9%)	49
	V_{In}-rich-ZIS	V_{In}	300 W Xe lamp AM 1.5 cut-off filter	45 mL acetonitrile (MeCN) + 5 mL trolamine (TEOA) + CO_2	CO: 298	51
	ZnM-LDH (M = Ti^{4+}, Ga^{3+}, Al^{3+})	M	300 W Xe lamp	0.1 mL H_2O + 0.08 MPa CO_2	CH$_4$: 1.2 (68% M = Ti), CO: 1.3 (90% M = Al), CO: 1.6 (78% M = Ga)	56
	CA@PCN-222	Zr^{III}-cluster	300 W Xe lamp (800 nm > λ > 400 nm)	60 mL mixed solution (MeCN/TEOA = 30/1) + CO_2	HCOO$^-$: 281.6	59
	UiO-Co-N3	Co-N3	300 W Xe lamp ($\lambda \geq$ 420 nm)	20 mL MeCN + 30 mg [Ru(bpy)$_3$]Cl$_2$·6H$_2$O + 0.025 M 1,3-dimethyl-1,3-dihydro-2-phenyl-2H-benzimidazole (BIH) + CO_2	CO: 179.3 (99.3%)	61
	Incorporating Cu sites into the connected nodes of defective UiO-66-NH$_2$	NH$_2$-Cu-NH$_2$	300 W Xe lamp (λ > 420 nm)	2 mL H_2O + 6 mL N,N-dimethylformamide (DMF) + CO_2	CH$_3$COCH$_3$: 70.9 (97%)	62
	2,2'-Bipyridine-based COF bearing non-noble single Cu sites	Cu^{2+} sites	300 W Xe lamp (λ > 420 nm)	10 mL DMF or H_2O + 1 mL triethylamine + CO_2	CH$_4$: 17.5; CO: 1.6 (H$_2$O), CO: 10.2 (100%; DMF), CO: 22.5 (66.4%; DMF/H$_2$O = 50%)	63
	Cu-COF	Cu–O/N sites	300 W Xe lamp (λ > 420 nm)	12 mL mixed solution + 600 torr CO_2, MeCN/H$_2$O/TEOA (8 mL/2 mL/2 mL)	CO: 206 (94%)	64
	Co-2,3-DHTA-COF	Co–O$_4$ sites	300 W Xe lamp (λ > 420 nm)	46 mL mixed solution + 10 mg [Ru(bpy)$_3$]Cl$_2$·6H$_2$O + 1 atm CO_2, MeCN/H$_2$O/TEOA (32 mL/8 mL/6 mL)	CO: 18 000 (95.7%)	65
	Mo-COF	MoN$_2$ sites	300 W Xe lamp ($\lambda \geqq$ 420 nm)	5 mL H_2O + 1 mL CO_2	CO: 6.19, C$_2$H$_4$: 3.57, CH$_4$: 1.08	66
	O/La-CN	La–N charge-transfer bridge	Xe lamp	12 mL mixed solution + 1 atm CO_2MeCN/H$_2$O/TEOA (6 mL/4 mL/2 mL)	CO: 92 (80.3%)	67
	Cu$_1$@BiOBr	Isolated Cu sites	300 W Xe lamp	5 mL H_2O + 4 MPa CO_2	CH$_3$OH: 627.66 (86.6%)	68
	[CoN$_3$O]ClO$_4$	Co(II) catalytic center	300 W Xe lamp (λ > 420 nm)	5 mL mixed solution + [Ru(bpy)$_3$]Cl$_2$·6H$_2$O + BIH + CO_2, MeCN/H$_2$O (4 mL/1 mL)	CO: 88.14% ± 2.09%	72
	CuNi-L^2	Active Ni^{II} site	LED light (λ > 420 nm)	25 mL mixed solution + [Ru(bpy)$_3$]Cl$_2$·6H$_2$O (0.85 mmol L^{-1})+ Triisopropanolamine (TIPA 0.8 mol L^{-1}) + CO_2, MeCN/H$_2$O (20 mL/5 mL)	CO: (93.5%)	73
	Cu single atoms on the nitrogen-doped carbon anchored on TiO$_2$	Cu SAs	300 W Xe lamp	H_2O vapor + CO_2	CO: 65.8	77
	2Re-In$_2$O$_3$	O$_{def}$	300 W Xe lamp (λ > 420 nm)	100 mL H_2O + 1.01 bar CO_2	CH$_3$OH: 265.6 (100%)	78
	Cu$_1$/TiO$_2$	Cu$_1$–O$_{2+1}$	Xe lamp	20 mL H_2O + TEOA + CO_2	C$_2$H$_4$: 60.4 (75.2%)	79
	MIL-88B-NS40	Fe–N coordinated sites/uncoordinated S	300 W Xe lamp (λ > 420 nm)	2 mL H_2O + CO_2	C$_2$H$_4$: 17.7	80
	B-Ni$_1$/WO$_{2.72}$	Ni site	300 W Xe lamp (λ > 420 nm)	6 mL mixed solution + 15 mg [Ru(bpy)$_3$]Cl$_2$·6H$_2$O + CO_2, MeCN/H$_2$O/TEOA (3 mL/2 mL/1 mL)	CO: 80 500 (98.7%)	82
	Isolated Mn atoms over the multi-edged TiO$_2$ nano-pompons	Mn atoms	300 W Xe lamp (λ > 400 nm)	6 mL mixed solution + 10 mg [Ru(bpy)$_3$]Cl$_2$·6H$_2$O + 1 atm CO_2, MeCN/H$_2$O/TEOA (3 mL/2 mL/1 mL)	CO: 80 510, H$_2$: 23 070	83
	In-bonded N-atom (In$^{\delta+}$-N$_4$) in the (002) crystal planes of g-C$_3$N$_4$	In$^{\delta+}$-N$_4$	300 W Xe lamp	400 μL H_2O + CO_2	CO: 398.87	84

Table 1 (Contd.)

	Catalyst	Reactive sites	Light source	Reaction condition	Performance (μmol g^{-1} h^{-1})	Ref.
	CuACs/PCN	Cu–N$_4$ sites doped P	300 W Xe lamp ($\lambda \geq$ 420 nm)	5 mL TEOA + [Ru(bpy)$_3$]Cl$_2$·6H$_2$O + 45 mL H$_2$O + CO$_2$	C$_2$H$_4$: 10.17 (53.2%), CH$_4$: 9.55	85
	3Er–ZnIn$_2$S$_4$	Er	300 W Xe lamp (λ > 420 nm)	TEOA + 100 mL H$_2$O + 80 kPa CO$_2$	CH$_4$: 6.68 (>90%)	86
	Cu$_1$N$_3$@PCN	Different coordination structures Cu-atom	300 W Xe lamp (λ > 420 nm)	1 mL H$_2$O + CO$_2$	CO: 49.8	87
	Ag$_1$@PCNT	Ag–N$_3$, Ag single atoms	300 W Xe lamp AM 1.5 cut-off filter	3 mL H$_2$O + 70 kPa CO$_2$	CO: 160 (>94%)	88
	Ultra-high Pr loading CN	Pr$_1$–N$_4$O$_2$ sites	300 W Xe lamp	1.0 mL H$_2$O + 4.0 mL CO$_2$	CH$_3$OH: 511.1	89
	MCOF-Ti$_6$Cu$_3$	Cu cluster	Xe lamp AM 1.5 cut-off filter	30 mL H$_2$O + CO$_2$	HCOOH: 169.8	90
Dual MAS	Mn$_1$Co$_1$/CN	Two compatible active centers of Mn and Co	300 W Xe lamp (λ > 400 nm)	2 mL H$_2$O + 80 kPa CO$_2$	CO: 47	17
	Cu–Ti–V$_O$/Ti$_{0.91}$O$_2$-SL	Cu–Ti–V$_O$ unit	300 W Xe lamp (λ > 400 nm)	12.5 mL MeCN + 2.5 mL H$_2$O + 1 atm CO$_2$	C$_2$H$_4$: 7.6, C$_3$H$_8$: 13.8, CO: 18.6	46
	CuInP$_2$S$_6$ monolayer	Cu–In dual site	300 W Xe lamp AM 1.5 cut-off filter	0.4 mL H$_2$O + CO$_2$	C$_2$H$_4$: 20.89 (56.4%), CO: 8.59, CH$_4$: 6.22	55
	V into NiAl-LDH	V; lower-valence Ni	300 W Xe lamp (λ > 400 nm)	10 mL mixed solution + 0.005 mmol [Ru(bpy)$_3$]Cl$_2$·6H$_2$O + 1.8 bar CO$_2$ MeCN/H$_2$O/TEOA (6 mL/2 mL/2 mL)	CH$_4$: 217 (78.9%)	57
	Dispersed Co–Ru bimetal into conjugated porous carbon nitride polymer	Co sites; Ru sites	300 W Xe lamp	500 μL H$_2$O + 70–80 kPa CO$_2$	CO: 27.3	69
	Ru Cu single atom incorporated into polymeric carbon nitride	Ru–N$_4$ sites, Cu–N$_3$ sites	300 W Xe lamp	9 mL NaHCO$_3$ (3 M) + 1 mL TEOA + CO$_2$	CH$_4$: 154 (95%), CO: 2, H$_2$: 6	70
	Re-bpy/PTF(Cu)	Re-bpy sites; Cu single sites in PTF(Cu)	300 W Xe lamp (1100 nm > λ > 400 nm)	5 mL mixed solution + 1 atm CO$_2$ MeCN/TEOA (2.5 mL/2.5 mL)	C$_2$H$_4$: 73.2	74
	Cu–N$_2$–V	Cu$^+$/Cu^{2+}	300 W Xe lamp	21 mL DMF + 3 mL H$_2$O + 0.8 MPa CO$_2$	C$_2$H$_5$OH: 69.8	81
	LaNi-Phen/COF-5	Optically active (La site) catalytically active (Ni site)	300 W Xe lamp	10 mM BIH + 48 mL MeCN + 2 mL H$_2$O + 80 kPa CO$_2$	CO: 605.8 (98.2%)	91
	CuIn$_5$S$_8$	Cu–In dual sites	300 W Xe lamp (λ > 400 nm)	2 mL H$_2$O + 0.1 atm CO$_2$	CH$_4$: 8.7	92
	Ag$_2$Cu$_2$O$_3$	Cu–Ag Lewis acid–base dual sites	300 W Xe lamp	5 mLH$_2$O or 5 mL 0.2% methanol aqueous solution was injected + CO$_2$	CH$_4$: 3.6	93
	In/TiO$_2$-Vo	Vo-regulated In-Ti dual sites	Xe lamp (320 nm < λ < 780 nm)	H$_2$O + CO$_2$	CH$_4$: 35.49 (91.3%)	94
	Au/Co dual single atom loaded CdS NPs	Au/Co DSA	300 W Xe lamp	CO$_2$	CO: 64.1 μmol g^{-1}, CH$_4$: 7.7 μmol g^{-1}	95
	Vo-rich Zn$_2$GeO$_4$ nanobelts	Asymmetric Zn–O–Ge sites	Xe lamp light	12 mL H$_2$O + 0.03 vol% CO$_2$/Ar gas mixture	CH$_3$COOH: 12.7 (29.95%)	96
	Au–CeO$_2$	Au–O–Ce sites	300 W Xe lamp	5 mL H$_2$O + 80 kPa CO$_2$	CO: 11.07, C$_2$H$_6$: 11.07 (65.3%)	97
	InCu/PCN	In–Cu dual sites	300 W Xe lamp	24 mL DMF/H$_2$O (12.5 vol% H$_2$O) + 0.8 MPa CO$_2$		98
				1.0 mL H$_2$O + (CO$_2$-1%, N$_2$-99%)	C$_2$H$_5$OH: 28.5 (92%)	99

Table 1 (Contd.)

Category	Catalyst	Reactive sites	Light source	Reaction condition	Performance (μmol g^{-1} h^{-1})	Ref.
	Bi$_2$WO$_6$ nanosheets with Vo anchoring Au and Cu dual single atoms	Au–Cu dual-single-atom sites; Vo	300 W Xe lamp (780 nm > λ > 320 nm)		Total amount of production (CO, CH$_4$, C$_2$H$_4$, C$_3$H$_6$): 83.9	100
	2% Pd–Cu/TiO$_2$	Pd–Cu; Vo	300 W Xe lamp	15 mL H$_2$O + 0.5 MPa CO$_2$	CH$_3$OH: 71.84 (91.71)	101
	Single atoms of Ni/Co loaded on TiO$_2$	Ni Co single atoms	300 W Xe lamp	50 mL H$_2$O (0.1 M Na$_2$SO$_3$ + 0.2 M CsOH) + CO$_2$	CH$_3$COOH: 22.6, 71%	102
	Incorporated the redox-active Co^{2+}/Ni^{2+} centers into the chemically stable layered lead iodide hybrids	Co^{2+}/Ni^{2+}–O–Pb bimetallic catalytic sites	AM 1.5 G filter	1 mL H$_2$O + CO$_2$	C$_2$H$_5$OH: 24.9–31.4, 89.5–93.6%	
	g-C$_3$N$_4$/UiO-66(Zr/Ce)	N–Zr/Ce–O	300 W Xe lamp	15 mL MeCN + 15 mL H$_2$O + 101 kPa CO$_2$	CH$_3$OH: 54.71, C$_2$H$_5$OH: 38.10	103
	Cu-CuTCPP/g-C$_3$N$_4$	Cu$^{1+\delta}$	300 W Xe lamp (800 nm > λ > 360 nm)	400 μL H$_2$O + 200 μL TEA + 0.1 MPa CO$_2$	CO: 12.3, CH$_4$: 11.6, C$_2$H$_6$: 18.5	104
MAS combined with vacancies	P and Cu dual sites anchored on graphitic carbon nitride	P–N and Cu–N$_4$ dual sites	300 W Xe lamp	3 mL TEOA + H$_2$O + 0.65 atm CO$_2$	C$_2$H$_6$: 616.6	31
	1% Ru–TiO$_{2-x}$	Ru; Vo	300 W Xe lamp	0.14 g NaHCO$_3$ + N$_2$ + H$_2$O + H$_2$SO$_4$ (2 M)	CH$_4$: 31.63 (90.93%)	45
	A series of metastable WO$_3$ photocatalysts with the coexistence of S doping and Vo	W–S–W bridge; Vo	300 W Xe lamp	0.4 mL H$_2$O + CO$_2$	C$_2$H$_4$: 224.278, 87.6%	47
	Au atoms to ultrathin ZnIn$_2$S$_4$ nanosheets with Vs	Au$_1$–S$_2$	300 W Xe lamp (λ > 420 nm)	5 mL mixed solution + 10 mg [Ru(bpy)$_3$]Cl$_2$·6H$_2$O + 1 atm CO$_2$ MeCN/H$_2$O/TEOA (3 mL/1 mL/1 mL)	CH$_4$: 275 (77%)	52
	Vs-AgInP$_2$S$_6$ single atomic layer	Ag atoms; Vs	300 W Xe lamp	0.4 mL H$_2$O + CO$_2$	C$_2$H$_4$: 44.3 (73%)	54
	Mn dopants and Vo were engineered in Zn$_2$GeO$_4$ nanorods	Mn dopants and Vo	300 W Xe lamp	1 mL H$_2$O + CO$_2$	CO: 40.02 (82.9%)	105
	Cu$_1$/N$_{2C}$V-CN	Cu single atoms; N$_{2C}$ vacancies	300 W Xe lamp AM 1.5 cut-off filter	200 μL H$_2$O + 105 kPa CO$_2$	CO: 11.12	106
	CuGaS$_2$/Ga$_2$S$_3$ containing Vs	Cu–Ga metallic bond	300 W Xe lamp (λ > 420 nm)	3 mL H$_2$O + TEOA + 70 kPa CO$_2$	C$_2$H$_4$: 335.67 (93.87%)	107
	Cu$_{1.95}$S$_{1-x}$	Dual Cu and Vs	300 W Xe lamp AM 1.5 cut-off filter	1 atm CO$_2$	CH$_4$: 12.42	108
MAS synergizing with nanoparticles	CA/Ni$_1$Cu$_{NP}$ N–C	Cu nanoparticles; Ni single-atom sites; asymmetric Ni–N$_4$ sites	300 W Xe lamp (λ > 420 nm)	95 mL H$_2$O + 5 mL TEOA + 100 kPa CO$_2$	CH$_4$: 35.245, CO: 32.067, C$_2$H$_6$: 25.328	109
	Co$_1$Ag$_{(1+n)}$-PCN	Co–N$_6$–P bonds, Ag–N$_2$C$_2$ SA sites, Ag NPs	300 W Xe lamp	6 mL CH$_3$CN + 4 mL H$_2$O + 80 kPa CO$_2$	CO: 46.82 (70.1%)	110
	Cu single atoms and nanoclusters supported on defective TiO$_2$	Cu SAs, Cu NCs	300 W Xe lamp	100 μL H$_2$O + CO$_2$	CH$_4$: 19.63 (98%)	111
	single Pd atoms and Pd nanoparticles on graphitic carbon nitride	Pd$_1$ sites; Pd$_{NPs}$ sites	Xe lamp	10 mL H$_2$O + 1 atm CO$_2$	CH$_4$: 20.3 (97.8%)	112
MAS within heterostructure	g-C$_3$N$_4$/CoCo-LDH	Co–N$_2$ bonds	300 W Xe lamp	3 mL H$_2$O + 1 atm CO$_2$	CO: 71.39	58
	CuO/Cu$_2$V$_2$O$_7$	Two metal atomic sites of Cu and V	300 W Xe lamp	20 mL TEOA + 80 mL H$_2$O + 1.01 bar CO$_2$	CO: 118, C$_2$H$_4$: 29.57	113
	2D/2D Ni-doped CsPbBr$_3$/Bi$_3$O$_4$Br Z-scheme heterojunction	Ni^{2+}	300 W Xe lamp	2 mL H$_2$O + 101 kPa CO$_2$	CO: 96.89 (98.2%)	114
	Co-TCPP/Bi$_3$O$_4$Br	Bi–O bridge bond; Co atoms	300 W Xe lamp	50 mL H$_2$O + 0.08 MPa CO$_2$	CO: 71.3	115

Table 1 (Contd.)

Catalyst	Reactive sites	Light source	Reaction condition	Performance (μmol g^{-1} h^{-1})	Ref.
Cu-SAEB	N–Cu$_1$–S single-atom electron bridge	300 W Xe lamp	0.1 mL H$_2$O + CO$_2$	CO: 236.0, O$_2$: 120.1	116
In$_2$O$_3$/CdSe-diethylenetriamine	In–O–Cd bonds; Vo	300 W Xe lamp	120 mg NaHCO$_3$ + 0.5 mL H$_2$SO$_4$	CO: 70.08, CH$_4$: 27.92	117
2D/0D g-C$_3$N$_4$/Cu$_2$SnS$_3$	Cu–C and Cu–N dual chemical bond; Cu sites	100 W Xe lamp AM 1.5 filter	H$_2$O + CO$_2$	CO: 18.2	118
NiAl–Fe–TCPP	Fe; Ni	300 W Xe lamp	0.005 mmol [Ru(byp)$_3$]Cl$_2$·6H$_2$O + 10 mL mixed solution + 1.8 bar CO$_2$ MeCN/H$_2$O/TEOA (6 mL/2 mL/2 mL)	C$_2$H$_4$: 2470	119
r-In$_2$O$_3$/InP	O–In–P polarized sites	300 W Xe lamp (λ > 420 nm)	100 mL H$_2$O + 80 kPa CO$_2$	CH$_3$COOH: 9.67 (96.1%)	120
CdS:Dy^{3+}/g-C$_3$N$_4$	Dy^{3+} single atom	300 W Xe lamp (λ > 400 nm)	4 mL H$_2$O + CO$_2$	CH$_4$: 8.06	121
Bi NCs/Bi$_2$O$_3$	Bi^0 of Bi NCs	300 W Xe lamp (λ > 420 nm)	1 mL H$_2$O + 0.08 MPa CO$_2$	CH$_4$: 7.45 (94.8%)	122
CsCuCl$_3$/Cu NCs	Cu NCs	150 W Xe lamp AM 1.5 cut-off filter	4 mL ethyl acetate (EA) + 1 mL propan-2-ol (IPA) + CO$_2$	CH$_4$: 7.2 (92.7%)	123

MAS as cocatalysts

Catalyst	Reactive sites	Light source	Reaction condition	Performance (μmol g^{-1} h^{-1})	Ref.
Ultrathin Bi$_{12}$O$_{17}$Cl$_2$ nanosheets	Vo; Bi clusters	300 W Xe lamp	50 mL H$_2$O + 0.08 MPa CO$_2$	CO: 64.3	124
Bi–BiOCl plasmonic nanoparticles decorated TiO$_2$ nanosheets	Bi	300 W Xe lamp AM 1.5 cut-off filter	5 mL 0.2 M NaHCO$_3$ + CO$_2$	CH$_3$OH: 235.78 ($\approx$90%)	125
Au/TiO$_2$/W$_{18}$O$_{49}$	Au–O–Ti, W–O–Ti	300 W Xe lamp (λ > 420 nm)	0.1 mL H$_2$O + CO$_2$	CH$_4$: 35.55, CO: 2.57, CH$_4$ (93.3%)	126
PtAg-2/HNb$_3$O$_8$	Pt–Ag alloy (7:43 Pt–Ag molar ratio)	300 W Xe lamp (320 nm < λ < 780 nm)	2 mL H$_2$O + 0.09 MPa CO$_2$	CH$_4$: 93.6 (74.3%)	127
PtCu/TiO$_2$	Pt/Cu alloy (0.4:0.6)	300 W Xe lamp (300 nm < λ < 400 nm)	Water vapor + CO$_2$	CH$_4$: 100%	128
Cu–Ag/TiO$_2$	Cu–Ag alloy (0.8:0.2)	300 W Xe lamp AM 1.5 cut-off filter	150 mL H$_2$O + 90 kPa CO$_2$	C$_2$H$_4$: 1110.6	129
AuIr with InGaN nanowires on silicon	Au$_3$Ir$_1$ alloy (0.44:0.56)	300 W Xe lamp	30 mL H$_2$O + 2 atm CO$_2$	C$_2$H$_6$: 58 800, CH$_4$: 125 400, H$_2$: 735 600, CO: 127 800	130
Au/TZO	Au nanoparticles	300 W Xe lamp AM 1.5 G filter	20 mL mixed solution + 1 atm CO$_2$ MeCN/H$_2$O/TEOA (16 mL/2 mL/2 mL)	H$_2$: 271.6, CO: 260.6, C$_2$H$_4$: 6.80, C$_2$H$_6$: 4.05	131
Bi nanoparticles grown on the Bi$_2$MoO$_6$ with Vo	Bi nanoparticles Vo	Xe lamp	0.42 g NaHCO$_3$ + 30 mL H$_2$O + CO$_2$	C$_2$H$_5$OH: 17.93 (92%)	132

CO_2, where the strong hybridization of the Cu 3d and CO_2-O 2p orbitals facilitated the transfer of electrons from the Cu single atoms to CO_2, effectively optimizing the rate-limiting step (CO_2* → COOH*). Moreover, single MAS also improved the selectivity of the liquid product of the photocatalytic CO_2 reduction. The atomically dispersed rhenium (Re) in In_2O_3 changed the product from CO on pure In_2O_3 to CH_3OH on 2Re-In_2O_3.[78] DFT calculations disclosed that the Re site promoted the H_2O dissociation to form sufficient H atoms for CO_2 reduction. Critically, CO preferred to be hydrogenated into CHO instead of desorption due to the strong binding between CO and Re_1-In_2O_3(111). Through multi-step hydrogenation, CHO was eventually converted to CH_3OH with high selectivity.

Photocatalytic CO_2 conversion mainly involves C=O bond cleavage and C–H bond formation, accompanied by the challenging C–C coupling toward the generation of C_{2+} products. The MAS could reduce electrostatic repulsion between the C_1 intermediates, promote C–C coupling, and thus lead to the highly selective formation of the C_{2+} product. The photogenerated electron transition from TiO_2 to atomically dispersed Cu atoms rearranged the energy levels of the Cu 3d orbitals.[79] Consequently, the initial four-coordinated Cu_1–O_4 was distorted into a Cu_1–O_{2+1} structure (twofold normal Cu–O coordination and one stretched Cu–O coordination), which could be reversibly recovered after removing the synergistic light field. The photoinduced metastable intermediate of Cu_1–O_{2+1} delivered an C_2H_4 yield rate of 60.4 µmol $gcat^{-1}$ h^{-1}. The energy barrier of the first protonation step from CO_2 to *COOH showed an obvious decline over Cu_1–O_{2+1}, indicating the stronger activation capability of the metastable asymmetrical structure to reactants than that of Cu_1–O_4. *CO molecules adsorbed more strongly on the Cu_1–O_{2+1} (−1.49 eV) surface than on the Cu_1–O_4 (−0.44 eV) surface, leading to subsequent hydrogenation rather than desorption. It was noteworthy that, in contrast to Cu_1–O_4, Cu_1–O_{2+1} promoted C–C coupling and further formation of C–C bonds, thus facilitating the generation of C_2H_4. Furthermore, N,S-codoped Fe-MOF MIL-88B with a well-defined bipyramidal hexagonal prism shape was designed.[80] The synergistic effect of the Fe–N coordinated sites and reasonable defects from uncoordinated S increased the electron density disorder around Fe, accelerated the migration of photogenerated carriers, benefited electron storage, and effectively promoted the formation of C–C coupling intermediates for C_2H_4. For liquid products, the carbon nitride-supported Cu single-atom catalyst with a defective low-coordination Cu–N_2 motif (Cu–N_2–V) exhibited superior photocatalytic activity for CO_2 reduction to ethanol relative to Cu–N_3 and Cu–N_4.[81] In particular, Cu in Cu–N_2–V existed in both Cu^+ and Cu^{2+} valence states. On the one hand, the Cu^+ sites benefited CO_2 activation. On the other hand, the coexistence of Cu^+/Cu^{2+} sites contributed to the strong adsorption of *CO and subsequent *CO–*CO dimerization. Finally, ethanol was ultimately produced from *CO–*CO, which underwent a series of hydrogenation processes.

The d-band center tuning strategy influences the carrier transportation and the adsorption of the reactant and intermediate to promote photocatalytic CO_2 conversion, which can be achieved by incorporating MAS. Bulk doping of single Ni atoms in $WO_{2.72}$ (B-Ni_1/$WO_{2.72}$) displayed superior solar-driven CO_2 reduction performance to surface anchoring of single Ni atoms on $WO_{2.72}$ (S-Ni_1/$WO_{2.72}$).[82] The introduction of Ni atoms led to an upward shift of the d-band center of W atoms in the $WO_{2.72}$ host structure due to the overlapping orbital hybridization. Critically, the d-band center of W in B-Ni_1/$WO_{2.72}$ shifted upward to a greater extent relative to S-Ni_1/$WO_{2.72}$. Therefore, the Ni atoms in B-Ni_1/$WO_{2.72}$ exhibited stronger electronic interactions with the $WO_{2.72}$ host, facilitating the formation of charge-transfer channels that enabled the rapid transfer of photogenerated electrons to the surface Ni atoms. Moreover, the free energies of *CO_2, *COOH, and *CO intermediates of B-Ni_1/$WO_{2.72}$ were integrally decreased compared to those on S-Ni_1/$WO_{2.72}$, benefiting the conversion of CO_2 to CO. Analogously, the decoration of isolated Mn atoms over the multi-edged TiO_2 nano-pompons shifted the d-band center upwards and pushed the antibonding orbital closer to the Fermi level, thus facilitating CO_2 adsorption.[83] The Mn site acted as an active center for CO_2 activation, and significantly reduced the formation energy barriers of *COOH to accelerate the decisive step of the reaction.

Besides in-plane regulation, MAS can realize interlayer-spacing adjustment, which may significantly influence the carrier transport of the bulk-catalyst, thereby affecting CO_2 photoreduction. Single-atom In-bonded N-atom ($In^{\delta+}$-N_4) in the (002) crystal planes of g-C_3N_4 reduced the (002) interplanar spacing of g-C_3N_4, benefiting the separation of bulk carriers.[84] More charges were transferred to the adsorbed CO_2 molecule from the $In^{\delta+}$-N_4 active center (0.116 eV) compared to the bare C_3N_4 site (0.006 eV), which was favorable for CO_2 adsorption. Moreover, the $In^{\delta+}$-N_4-led CO_2 hydrogenation to *COOH was downhill by −0.114 eV and evidently surpassed the uphill step by 2.09 eV on the bare C_3N_4, which optimized the reaction path.

3.2 Dual MAS

The precise construction of photocatalysts with dual MAS to achieve the simultaneous fostering of light absorption and catalytic activity is a formidable challenge. The bifunctional LaNi sites within COF were synthesized by electrostatically driven self-assembly approach.[91] The La–Ni dual MAS accelerated the dynamic behavior of the photogenerated charge carriers, comprising photoelectron transfer from La-Phen to the COF-5 colloid and subsequent electron injection into Ni-Phen for the CO_2 reduction process. In addition, the bimetallic LaNi coordination facilitated the generation of abundant *COOH groups, and effectively decreased the activation barrier of CO_2 transformation. Moreover, the CO desorption was thermodynamically preferred over CHO* formation, with an energy barrier of 0.72 eV versus 1.02 eV, resulting in high CO selectivity.

Precise control of the formation of $Metal_1$⋯C=O⋯$Metal_2$ (M_1⋯C=O⋯M_2) intermediates at the photocatalyst interface is one of the critical steps in the formation of hydrocarbons. This is due to the fact that the energy required for simultaneous cleavage of the M_1⋯O and M_2⋯C bonds is much greater than that required for C–O bond breaking (Fig. 9a).[92] $Ag_2Cu_2O_3$
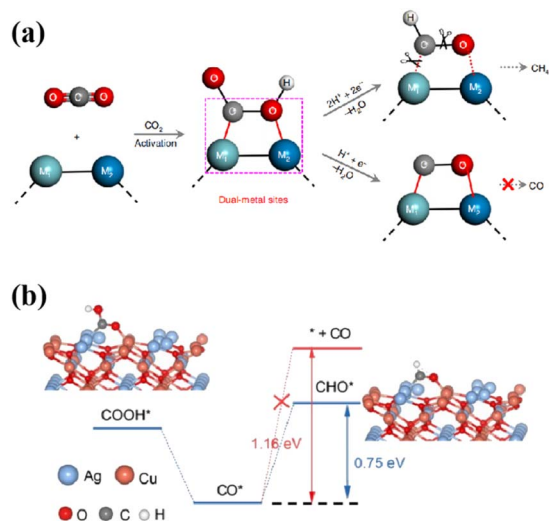
Fig. 9 (a) CO_2 photoreduction into fuels such as CH_4 and CO through the use of dual-metal-site catalytic systems (M represents the metal site, 'H$^+$ + e$^-$' refers to the proton coupled electron transfer process and '$-H_2O$' means the desorption of H_2O molecules after the intermediates react with the proton–electron pair). This figure has been reproduced from ref. 92 with permission from Springer Nature, copyright 2019. (b) The rate-determined step of photoreduction of CO_2 into CH_4 over $Ag_2Cu_2O_3$ nanowires. This figure has been reproduced from ref. 93 with permission from Wiley-VCH, copyright 2023.

nanowires with abundant Cu–Ag Lewis acid–base dual sites on the preferentially exposed (110) surface were utilized as a model catalyst to achieve 100% selectivity in the photogeneration of CH_4 from CO_2.[93] The Cu···Ag Lewis acid–base dual sites on $Ag_2Cu_2O_3$(110) regulated the M_1···C=O···M_2 intermediate formation, converting CO_2 into hydrocarbons. The rate-determining step with a corresponding Gibbs free energy (ΔG(CHO*)) of 0.75 eV led to greater feasibility in CO* forming CHO* than desorbing from the catalyst surface (1.16 eV, Fig. 9b). Similarly, the highly stable Cu–C–O–In intermediate at the Cu–In dual sites of the sulfur-deficient $CuIn_5S_8$ converted the endoergic protonation step to an exoergic reaction process, changing the reaction pathway to form CH_4 instead of CO.[92] Furthermore, the V_O-regulated In–Ti dual sites enabled the formation of a stable adsorption conformation of the In–C–O–Ti intermediate, leading to the highly selective reduction of CO_2 to CH_4.[94]

Catalysts containing dual MAS regulates the electron distribution by creating asymmetric atomic configurations, which significantly affects the photocatalytic performance, especially for multi-electron CO_2 reduction. The mechanism of reverse electron transfer over Au and Co bimetallic atom catalysts was reported.[95] Electrons were delocalized from Au and accumulated around the Co atoms, resulting in the electron-rich Co atoms adsorbing/activating CO_2 molecules readily, which significantly promoted photocatalytic CO_2 reduction. In this regard, the Au/Co double single-atom loaded CdS increased the yield of CO and CH_4 by nearly 2800% and 700%, respectively, compared to CdS alone. In addition, the disparate electron distributions and valence states of two distinct metal atoms

could endow significantly different charge distributions of the neighboring C_1 intermediates to effectively suppress the electrostatic repulsion. The asymmetric Zn–O–Ge triatomic sites in the V_O-rich Zn_2GeO_4 nanobelts induced distinct charge distributions of neighboring C_1 intermediates, which facilitated the C–C coupling with a high CO_2-to-CH_3COOH conversion rate of 29.95%.[96] Under similar mechanisms, incorporating redox-active Co^{2+}/Ni^{2+} cations (TM) into layered lead iodide hybrids (TJU-39(Pb)) achieved efficient photocatalytic CO_2-to-C_2H_5OH conversion (yield of 24.9–31.4 μmol g^{-1} h^{-1}, selectivity exceeding 90%).[102] It was experimentally demonstrated that the interlayer TMs were delocalized to the lead iodide layers to construct TM–O–Pd sites with substantial asymmetric charge distribution, which reduced the reaction barrier for C–C coupling. Specifically, the two-electron reduction of CO_2 to CO* occurred simultaneously at the charge-enriched Pb^{2+} sites and the Ni^{2+} site, which subsequently underwent C–C coupling to form OC–CO* intermediates. The OC–CO* intermediate coupled multiple e$^-$/H$^+$ pairs, combining the dehydration process to finally yield C_2H_5OH.

From an overall reaction perspective, the CO_2 photoreduction contains oxidation and reduction half-reactions, involving multiple proton-coupled electron transfer processes. The MAS construction not only enhances CO_2 reduction, but also influences the corresponding oxidation half-reaction. The existence of an internal electric field pointing from the Ti cluster to the Cu cluster in MCOF-Ti_6Cu_3 facilitated carrier separation, leading to electron and hole transfer to the Cu cluster and Ti cluster, respectively.[90] Consequentially, electrons reaching the Cu cluster drove the reductive reactions, and the oxidative reaction proceeded at the Ti cluster. Analogously, two compatible active centers of Mn and Co were loaded onto carbon nitride (Mn_1Co_1/CN).[17] The active center of Mn promoted H_2O oxidation by accumulating photogenerated holes, along with Co-facilitated CO_2 activation by increasing the bond length and bond angle of CO_2 molecules.

3.3 MAS combined with vacancies

Vacancies exhibit great influence on the properties of MAS. V_O-containing Co_3O_4 hollow nanoparticles loaded on a macro-porous N-doped carbon framework realized the photoreduction of low-concentration CO_2 to CO.[133] V_O distorted the nearby Co–O bonds, broke the local structural symmetry of the Co–O–Co sites, and thus caused an asymmetric distribution of charge density compared with pristine Co_3O_4. This asymmetrical active site with a polarized electronic structure endowed a stronger electrostatic interaction between the CO_2 molecule and V_O, which switched the CO_2 configuration from a single-site linear model to a multiple-sites bending one, therefore facilitating CO_2 activation. Moreover, the hydrogenation of adsorbed *CO_2 proceeded smoothly on the V_O-Co_3O_4 surface, and the adsorption capacity of *COOH was obviously stronger than that of Co_3O_4. Mn dopants and V_O were engineered in Zn_2GeO_4 nanorods (denoted as Mn-ZGO-V_O), which exhibited prominent photocatalytic CO_2 reduction performance.[105] The introduction of V_O in Mn-ZGO-V_O caused the charge accumulation on the Mn

atoms near Vo, certainly favoring the electron-rich Mn sites for CO_2 molecule capture. The lattice strain and ligand effects caused by Mn doping and Vo engineering elevated the d-band centers, endowing less filling of the antibonding states and hence stronger binding strength of CO_2. Moreover, the formation of COOH* on the Mn-ZGO-Vo slab changed from endothermic to exothermic, and the rate-limiting step was tuned to CO* formation with a lowest energy barrier among ZGO and Mn-ZGO. Precisely constructed Cu single-atom centers and two-coordinated N vacancies as dual active sites on carbon nitride (Cu_1/N_2CV-CN) achieved a high carbon-based selectivity of 98.50% for CO production.[106] The atomic Cu active sites promoted the chemisorption of CO_2 by changing the electronic structure of the surface. The N_2C vacancy became the active site for the adsorption of H_2O, which accelerated the dissociation of H_2O by reducing the dissociation energy barrier of H_2O from 2.59 eV to 1.68 eV. Moreover, the decrease in the rate-limiting step (the formation of COOH* species) by the dual active sites in Cu_1/N_2CV-CN led to a decent CO production rate of 11.12 $\mu mol\ g^{-1}\ h^{-1}$.

The geometry of MAS regulated by vacancies ultimately affects the catalytic performance to generate C_{2+}. Ultra-thin $CuGaS_2/Ga_2S_3$ containing Vs realized the selectivity of C_2H_4, reaching $\approx 93.87\%$ with the yield of $\approx 335.67\ \mu mol\ g^{-1}\ h^{-1}$.[107] Vs induced a highly delocalized electron distribution in the original region of S atoms, forming a Cu–Ga metallic bond. The upshift of the d-band center of Cu–Ga ions induced by Vs could not only enforce the adsorption ability for the intermediates of *CHOH*CO to initiate C–C coupling, but also accumulate electrons to drive the kinetic process of photocatalytic CO_2 reduction.

3.4   MAS synergizing with nanoparticles

The synergistic effect of MAS and nanoparticle accelerates the complex activation and hydrogenation process of photocatalysis. Introducing such a complex structure for simultaneous CO_2 reduction and H_2O dissociation is still a formidable challenge, and its underlying mechanism remains to be elucidated. The nitrogen-doped carbon anchoring with Cu nanoparticles and Ni single-atom sites (Ni_1Cu_{NP} N–C) were hybridized with CoAl-LDH (CA) for photocatalytic CO_2 reduction (CA/Ni_1Cu_{NP} N–C).[109] The photogenerated electrons of CoAl-LDH were transferred to N–C in the presence of the internal potential, and eventually accumulated on dispersed Ni single-atom sites. Meanwhile, the loading of Cu nanoparticles could significantly facilitate this charge transfer. The Ni center showed a high charge density, which facilitated reactant/intermediate adsorption and promoted catalytic reactions with multi-electron participation. Furthermore, the charge density around the electron-rich center $Ni-N_4$ showed an asymmetric distribution in the presence of Cu nanoparticles. This asymmetric active site was favorable for coupling adjacent *CO, thus promoting the generation of C_2 products. A cooperative catalyst containing Ag nanoparticles with adjacent atomic cobalt–silver dual-metal sites on P-doped carbon nitride ($Co_1Ag_{(1+n)}$-PCN) was reported for photocatalytic CO_2

reduction.[110] The asymmetric $Co–N_6–P$ sites coupled with $Ag–N_2C_2$ sites could serve as the charge transfer channel to facilitate the migration of electrons to the surface reaction sites, while Ag nanoparticles acted as the electron acceptor to enrich and separate photogenerated electrons. Moreover, the synergistic function of Ag nanoparticles with adjacent atomically dispersed $Ag–N_2C_2$ and $Co–N_6–P$ single-atom sites promoted the adsorption of CO_2 molecules onto the photocatalyst surface, and facilitated the formation of CO_2* and COOH*.

3.5   MAS within a heterostructure

The construction of heterogeneous structures enhances light absorption and provides sufficient reaction sites.[44] In addition, the heterostructure can realize the spatial separation of the reduction and oxidation reaction sites, improving the utilization rate of the photogenerated carrier and preserving high-energy electrons and holes. MAS is conducive to the tight connection of heterogeneous structures and promotes the directional carrier transportation. The presence of Vo exposed Bi atoms on the Bi_3O_4Br surface, which formed an interfacial Bi–O bond by grafting the terminal O of the cobalt porphyrin (Co-TCPP).[115] The Bi–O bond, as a charge-transfer bridge, promoted the extraction and transfer of photogenerated electrons from the external $[Bi_3O_4]$ layers to Co-TCPP. This contributed an effective space charge separation and the slow recombination process on the μs–ms time scale of CoTCPP. MoS_2 decorated with Cu species (Cu_1/MS) was coated on the surface of $MIL-125-NH_2$ (MIL), which constructed a $N–Cu_1–S$ single-atom electron bridge (denoted as Cu-SAEB).[116] The Cu-SAEB achieved a Z-scheme charge-transfer mode between Cu_1/MS and MIL, thus prolonging the lifetimes of carriers with a strong redox potential. Benefiting from the strengthened contact interface of Cu-SAEB, the highly active and stable CO_2 reduction performance was achieved, with CO and O_2 formation rates of 236.0 and 120.1 $\mu mol\ g^{-1}\ h^{-1}$, respectively. Similarly, an In–O–Cd bond-modulated S-scheme heterojunction of In_2O_3/CdSe-diethylenetriamine accelerated the photogenerated electron transfer.[117] Combined with the electron capture effect of Vo in In_2O_3, the $In–Vo–In–O–Cd$ structural units at the interface led to the extraction of electrons and the rapid transfer to the surface-active sites, improving the electronic coupling of CO_2.

The interface of the heterostructure could natively provide MAS for photocatalytic reactions. For example, the unique Cu–C and Cu–N dual chemical bond at the interface of the fabricated $g-C_3N_4/Cu_2SnS_3$ nanocomposite led to a superior CO formation rate from CO_2 photoreduction.[118] The Z-scheme carrier conduction was highly activated due to the interfacial nitrogen vacancies via the Cu–C and Cu–N bonding for CO_2 reduction on the conduction band (CB) of Cu_2SnS_3 and water oxidation on the VB of $g-C_3N_4$. The more negative overall free energy of Cu sites relative to Sn and S implied that the CO_2 conversion reaction occurred mainly via effective dual bonds between Cu sites and the C and N elements in $g-C_3N_4$.[118]

Heterogeneous structures enriched with MAS can generate C_{2+} products. A novel supramolecular assembly of NiAl–Fe-TCPP obtained by intercalating iron porphyrin (Fe-TCPP) into

NiAl-layered double hydroxide (NiAl-LDH) exhibited superior catalytic performance of CO_2 photoreduction to derive C_2H_4 with high selectivity up to 93.4%.[119] The strong host–guest interaction between LDH and Fe-TCPP led to the electron transfer from NiAl-LDH to Fe-TCPP. According to the *ex/in situ* XAS, the valence of Fe decreased along with the increase of Ni valence compared with that of Fe-TCPP and LDH, respectively. The low valence of Fe in NiAl–Fe-TCPP facilitated the CO* hydrogenation and coupling with CHO* to form COCHO*. Particularly, the CO_2 activation to CO was accomplished on NiAl-LDH, and then spilled to Fe-TCPP and coupled to generate COCHO*, which was further hydrogenated to produce C_2H_4. The O–In–P polarized sites at the r-In_2O_3/InP interface promoted C–C coupling with a productivity of 96.7 μmol g^{-1} and selectivity >96% for CO_2 photoreduction to CH_3COOH.[120] The interfacial In atoms accumulated electrons and transferred electrons to CO_2, thus promoting CO_2 adsorption and activation. The quite different carbon Bader charges of OCCO* on r-In_2O_3/InP caused by the formation of rich O–In–P reactive sites at the interface alleviated dipole–dipole repulsion and promoted C–C coupling (Fig. 10a–c). Ultimately, the C–C coupling energy barrier of r-In_2O_3/InP (0.5461 eV) was lower than that of pure In_2O_3 (0.9446 eV), suggesting that the formation of heterostructures by modifying In_2O_3 with P favored the formation of C_{2+} products (Fig. 10d).

3.6 MAS as cocatalysts

The cocatalyst plays a crucial role in semiconductor-based photocatalysis, which is conducive to the migration of electrons or holes, and improves the utilization efficiency of the photogenerated carrier. Moreover, cocatalysts can reduce the activation energy and overpotential of the CO_2 conversion to speed up the surface reaction.[44] MAS used as cocatalysts can

effectively improve photocatalytic performance. Bi nanoclusters (NCs) were prepared *in situ* on Bi_2O_3 through dehalogenation of Bi_3O_4Br by regulating the pH value in the hydrothermal process.[122] The construction of Bi sites on the basis of Bi_2O_3 could promote photogenerated charge transfer through the Schottky junction. Moreover, the change of the valence state of Bi regulated the type of active sites from O of the original Bi_2O_3 to Bi^0 of the Bi NCs in Bi NCs/Bi_2O_3, thus regulating the path of CO_2 photoreduction. Thermodynamically, the *CO intermediate on the Bi site tended to hydrogenate to *CHO species, accompanied by a subsequent multi-step hydrogenation process that selectively generated CH_4 on Bi NCs/Bi_2O_3. The *CO desorption to form CO over Bi_2O_3 was spontaneous and exothermic, whereas the hydrogenation of *CO to form the *CHO species required overcoming a large energy barrier (2.29 eV), leading to CO being the only reduction product of Bi_2O_3. Similarly, the $CsCuCl_3$/Cu heterojunction synthesized *via* a simple acid-etching solution process exhibited high CH_4 selectivity.[123] The accumulating of charges at the contact interface between $CsCuCl_3$ and Cu nanocrystals formed a Schottky contact, facilitating the extraction of photoelectrons from $CsCuCl_3$ to Cu nanocrystals, thereby realizing the effective separation of photogenerated electron–hole pairs. Moreover, the Cu nanocrystals accelerated the photocatalytic CO_2 reduction toward CH_4 *via* manipulating the adsorption and activation of CO_2 and stabilizing the reaction intermediates.

The surface plasmon resonance of MAS plays a crucial role in the collection and conversion of solar energy by the strong local fields. The coexistences of Vo and Bi clusters generated *in situ* on ultrathin $Bi_{12}O_{17}Cl_2$ nanosheets contributed to the high efficiency of the CO_2-to-CO conversion.[124] The Bi clusters exhibited a plasmon effect that extended the light absorption and enabled more sunlight harvest. Furthermore, Bi clusters acted as hole trapping centres in synergy with Vo as electron trapping sites, leading to the spatial separation of photogenerated electron–hole pairs. As another example, the attachment of non-noble plasmonic Bi particles with BiOCl shells to self-assembled TiO_2 nanosheets created a transformative hybrid plasmonic nanostructure. Bi stabilized by the BiOCl shell generated robust localized surface plasmon resonances, inducing a local field enhancement of 7–9 times, thus enabling the efficient and selective CO_2-to-methanol conversion at the TiO_2–BiOCl heterointerfaces.[125] In addition, it is worth mentioning that the localized surface plasmon resonance effect of Bi nanoparticles could significantly improve the rate and selectivity of the C_2H_5OH generation.[132] The high localized electron density and abundance of hot electrons in the active site drove the multi-electron reduction reaction, favoring the generation of C_{2+} products.

Plasmon resonance-mediated photocatalysis on precious metal surfaces (mainly Ag and Au) shows great potential for solar energy harvesting and conversion. For instance, plasmonic Au mediated the S-scheme charge transfer, and generated additional energetic hot electrons and holes to inject to the CB of $ZnIn_2S_4$ and VB of CuS, respectively, enabling a more thorough separation of carriers for CO_2 reduction and H_2O oxidation.[134] Moreover, a new idea of plasmonic active "hot
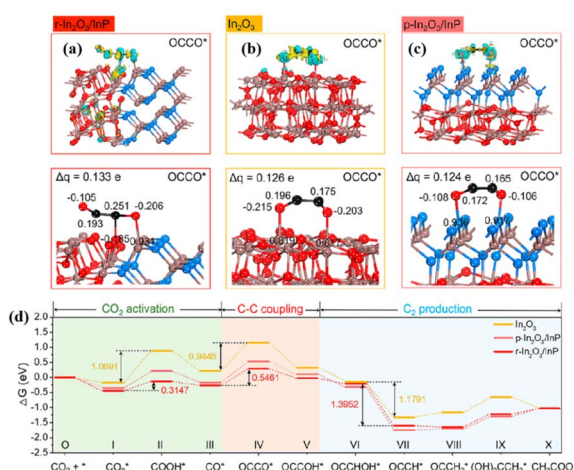

Fig. 10 Calculated electron density difference diagrams and the Bader charge values of (a) r-In_2O_3/InP, (b) In_2O_3, and (c) p-In_2O_3/InP with OCCO* absorbed. (d) Free energy diagrams for the reduction of CO_2 to CH_3COOH over r-In_2O_3/InP, In_2O_3, and p-In_2O_3/InP. These figures have been reproduced from ref. 120 with permission from American Chemical Society, copyright 2023.

spot"-confined photocatalysis was proposed to improve the photocatalytic CO_2 conversion. Specifically, tiny gaps (<10 nm) between the plasma nanostructures promoted plasma coupling between the nanostructures, resulting in the formation of classical "hot spots". The $Au/TiO_2/W_{18}O_{49}$ sandwich-like substructures with the short distance (<10 nm) between Au and adjacent $W_{18}O_{49}$ induced an intense plasmon-coupling to form the active "hot spots" in the substructures.[126] These active "hot spots" could gather the incident light to enhance "hot electron" generation and migration, and capture protons and *CO through the dual-hetero-active-sites (Au–O–Ti and W–O–Ti) at the $Au/TiO_2/W_{18}O_{49}$ interface, thus accelerating the protonation of *CO intermediates to derive CH_4.

Alloys as MAS enhance light absorption, inhibit charge recombination, and adsorb and activate reactants, thereby improving the selectivity of specific products. The PtAg alloy over HNb_3O_8 nanosheets trapped the electrons and improved the charge separation efficiency, mitigating the kinetical challenge of the eight-electron transfer process for CH_4.[127] In addition, the PtAg alloy acted as synergistic sites to reduce CO_2 to CO intermediates at the Ag site, which were then spilled over or sequentially adsorbed at neighboring Pt sites for further hydrogenation to CH_4. As another example, PtCu alloys with appropriate Pt/Cu ratios were deposited onto TiO_2 nanocrystals, which significantly improved CH_4 production with 100% selectivity.[128] The PtCu alloy effectively facilitated the separation/transfer of photogenerated charges, benefited the adsorption of CO_2, and promoted the formation and activation of intermediates (CO_2^-, *COOH, *CO, and *CHO). The synergistic effect of PtCu lowered the activation energy barriers of *CO_2 and *CHO, inhibited the desorption of *CO, and ultimately optimized the efficiency and selectivity of CH_4.

The alloy MAS promotes the C–C coupling and desorption of *C_2 intermediates from the catalyst surface. Loading Cu–Ag alloy sub-nanoclusters (ASNCs) on TiO_2 for CO_2 photoreduction produced C_2H_4 with a record-high formation rate (1110.6 $\pm$ 82.5 μmol g^{-1} h^{-1}).[129] The interaction between Cu and Ag in the Cu–Ag ASNCs promoted the C–C coupling of CH_2* at the Cu active site, which led to the spontaneous formation of *C_2H_4 from CH_2* on Cu–Ag alloy/TiO_2. In addition, the desorption energy of *C_2H_4 in the Cu–Ag alloy/TiO_2 was lower than that in Ag/TiO_2. This suggested that the interaction between Cu and Ag promoted the desorption of *C_2H_4, and thus the selective and efficient production of C_2H_4. Ag, in conjunction with Ir, achieved C–C coupling by inserting CO_2 into –CH_3, facilitating the formation of C_{2+} during CO_2 photoreduction.[130] Specifically, the assembly of AuIr with InGaN nanowires on silicon achieved a C_2H_6 activity of 58.8 mmol g^{-1} h^{-1} with a turnover number of 54 595 over 60 h. The Ir sites in Au–Ir alloys increased CO_2 reduction activity by lowering the reaction energy of key elementary steps (for example, CO_2 to *COOH on pure Au and *CO to *CHO on Au_3Ir_1 alloy) and steered the selectivity from the dominant HER to C–C coupling. The insertion of CO_2 into *CH_3 toward *CH_3COO exhibited the lowest reaction energy compared with other C–C coupling forms (CH + *CH → *C_2H_2, *CH_2 + *CH_2 → *C_2H_4, *CH_3 + *CH_3 → C_2H_6(g) and CO_2

insertion into *CH_3 to *CH_3COO), revealing the possible mechanism of C–C coupling for C_2H_6 synthesis.

4 Identification the role of MAS in photocatalysis

With the growing development in nanoscale characterization, a variety of techniques have emerged to assess the role played by MAS in photocatalysis. Specifically, microscopic visual characterization combined with spectroscopic measurements can help to reveal the structure and the coordination environments of the sample, along with the *in situ* observation of intermediary transformations to profoundly reveal the reaction mechanisms. In addition, theoretical calculations simulating the role of MAS in photocatalysis reveal the physical and chemical properties exhibited by MAS during CO_2 conversion.[135]

4.1 High-resolution aberration-corrected high-angle annular dark-field scanning transmission electron microscopy (AC-HAADF-STEM)

In the structural characterization of single-atom catalysts, high-resolution AC-HAADF-STEM demonstrates paramount importance in elucidating the distribution of the MAS and its geometry. Isolated Co single-atom-modified 2D monolayer ZIS nanosheet composites (Co-^{s}ZIS) possessed dual active centers of Co and Zn.[136] AC-HAADF-STEM was used to characterize the dispersion and configuration of the atoms involved, and to assist in determining the atomic structure of Co-^{s}ZIS. Fig. 11a clearly shows the distribution of isolated Co atoms in ^{s}ZIS, with the yellow circles marking the atomic spots that were brighter compared to the surrounding support. Fig. 11b and c reflects the fact that the corresponding atoms exhibited different
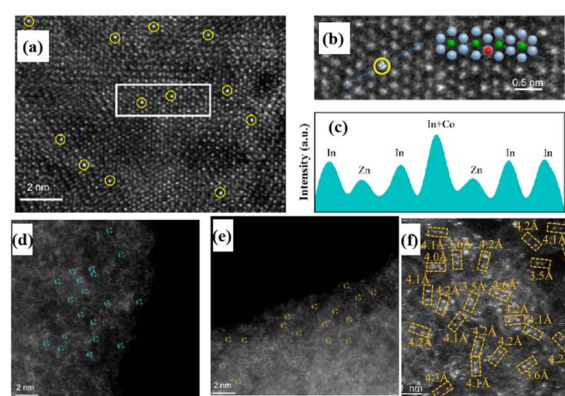

Fig. 11 (a) Aberration-corrected HAADF STEM image of the Co-^{s}ZIS; single-atomic Co sites are highlighted by yellow circles. (b) Magnified view of the white box in (a) (inset is the simulated atom distribution of Co-^{s}ZIS, and the green, gray, and red spheres represent the Zn, In, and Co atoms, respectively). (c) Intensity profile corresponding to the dark cyan arrow in (b). These figures have been reproduced from ref. 136 with permission from American Chemical Society, copyright 2023. Aberration-corrected HAADF-STEM images of (d) Ni–N–C, (e) Fe–N–C, and (f) (Ni, Fe)–N–C. These figures have been reproduced from ref. 137 with permission from Wiley-VCH, copyright 2023.

contrasts, with one of the largest peaks corresponding to the overlapping intensity spectra of an In atom and the individual Co atom. In addition, AC-HAADF-STEM was used to further examine the detailed distribution state of the MAS. The bright spots in Fig. 11d and e confirmed the isolated dispersion of Ni or Fe atoms on the carbon skeleton of the Ni–N–C and Fe–N–C single-atom catalysts, respectively, and no atom pairs were observed. In contrast, the AC-HAADF-STEM images of the (Ni, Fe) dual-single-atom catalysts (Fig. 11f) clearly showed most of the bright spots appearing in pairs, marked by yellow rectangles, confirming the formation of Ni/Fe dual-atom pairs with an average distance of about 4.1 Å.[137]

4.2 X-ray photoelectron spectroscopy (XPS)

XPS is considered to be an effective method to analyze the surface properties of the catalysts, reflecting the chemical bonding composition and the migration paths of carriers based on peak shifts. Porous covalent triazine frameworks (CTFs) were combined with CdS nanorods to obtain CdS@CTF-HUST-1 heterojunction photocatalysts with core–shell structures for CO_2-to-CO conversion.[138] Essentially, the full XPS spectra showed the coexistence of Cd, S, C and N elements in the CdS@CTF-HUST-1 with an optimal CdS content, referred to as Cd(0.9)@CTF. *In situ* XPS was conducive to revealing S-scheme charge transfer mechanisms of CdS@CTF-HUST-1. As shown in Fig. 12, the Cd 3d and S 2p peaks of the CdS(0.9)@CTF sample showed a positive displacement with respect to CdS, while the C 1s and N 1s peaks of CdS(0.9)@CTF exhibited a negative shift relative to CTF-HUST-1 under dark conditions. Such shifts indicated the interfacial transfer pathway of electrons from CdS to CTF-HUST-1. Under light illumination, the binding energies of Cd 3d and S 2p of the CdS(0.9)@CTF were negatively shifted compared to those in darkness, while the binding energies of C 1s and N 1s underwent positive
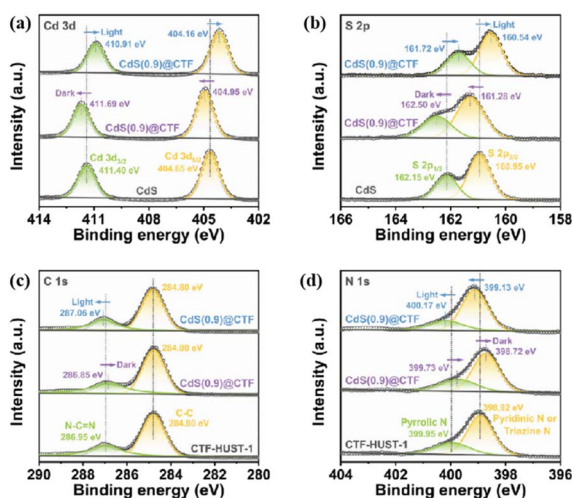

Fig. 12 High-resolution XPS spectra of (a) Cd 3d, (b) S 2p, (c) C 1s, and (d) N 1s of CdS, CTF-HUST-1, and CdS(0.9)@CTF samples. The *in situ* XPS measurement was performed under light irradiation. These figures have been reproduced from ref. 138 with permission from Wiley-VCH, copyright 2023.

displacement. These peak shifts confirmed that the internal electric field could drive the transfer of photogenerated electrons from CTF-HUST-1 to CdS under light irradiation. Furthermore, *in situ* irradiated XPS validated the Z-scheme charge transfer path of Ni-doped $CsPbBr_3/Bi_3O_4Br$ with an internal electric field directing from Ni-doped $CsPbBr_3$ to Bi_3O_4Br.[114] The binding energies of Cs, Pb and Br of $CsPbBr_3$ were all positively shifted upon Ni doping, suggesting that the introduced Ni sites interacted with the surrounding atoms to reduce the electron density around the Cs, Pb and Br atoms. After composing the heterostructure, the Cs 3d and Pb 4f of Ni-doped $CsPbBr_3/Bi_3O_4Br$ were shifted to higher binding energy by 0.3 eV with respect to Ni-doped $CsPbBr_3$, whereas Bi 4f and O 1s underwent a 0.2 eV shift to lower binding energy with respect to Bi_3O_4Br. In addition, the distance between the Br $3d_{5/2}$ and Br $3d_{3/2}$ peaks increased, indicating an enhanced spin–orbit splitting function of Br 3d. These results revealed changes in the charge loss and accumulation states of Ni-doped $CsPbBr_3$ and Bi_3O_4Br in the heterostructures, demonstrating the strong interfacial interaction between Bi_3O_4Br and Ni-doped $CsPbBr_3$. Upon illumination, Cs 3d and Pb 4f moved toward lower binding energies relative to the characteristic peaks in the dark environment, while Bi 4f and O 1s exhibited significant positive shifts. These results suggested that the light-induced electrons follow a Z-scheme path from Bi_3O_4Br to Ni-doped $CsPbBr_3$.

4.3 X-ray absorption fine structure (XAFS)

Based on synchrotron radiation, XAFS has become an important technique to reveal the electronic structure, coordination number and bonding environment of MAS, and is widely used to study MAS-containing catalytic systems. Specifically, the technique is usually classified into X-ray absorption near-edge structure (XANES) and extended X-ray absorption fine structure (EXAFS).[139]

Cu–N_4 sites-anchored phosphorus-modulated carbon nitride (CuACs/PCN) regulated the intermediate energy levels to achieve C_2H_4 formation during CO_2 photoreduction.[85] The Cu K-edge XANES of CuACs/PCN was between Cu_2O and CuO (Fig. 13a), indicating that the oxidation state of Cu is between +1 and +2. In the EXAFS spectrum (Fig. 13b), CuACs/PCN had a prominent peak near 1.5 Å, corresponding to the scattering of the Cu–N bond in the first coordination shell. The absence of the Cu–Cu coordination (2.2 Å) indicated that the Cu sites were atomically dispersed. From the fitting results (Fig. 13c), Cu atoms in CuACs/PCN were coordinated by four N atoms at a distance of 1.97 Å. The wavelet transform contour plot of CuACs/PCN exhibited a radial distance of 1.5 Å (*Y*-axis), which was significantly different from that of the Cu foil. These results strongly demonstrated that Cu atoms were dispersed with Cu–N_4 coordination in CuACs/PCN. In addition, XAFS was applied to study the coordination environment of MAS in $Co_1Ag_{(1+n)}$-PCN.[110] In the Ag K-edge XANES spectra, the near-edge absorption peak of $Co_1Ag_{(1+n)}$PCN was located above Ag_2O, indicating that the valence state of Ag was near +1 (Fig. 13e). Two main peaks at 1.5 and 2.4 Å in the Fourier-transformed Ag k^2-weighted EXAFS spectra (Fig. 13f) corresponded to the first
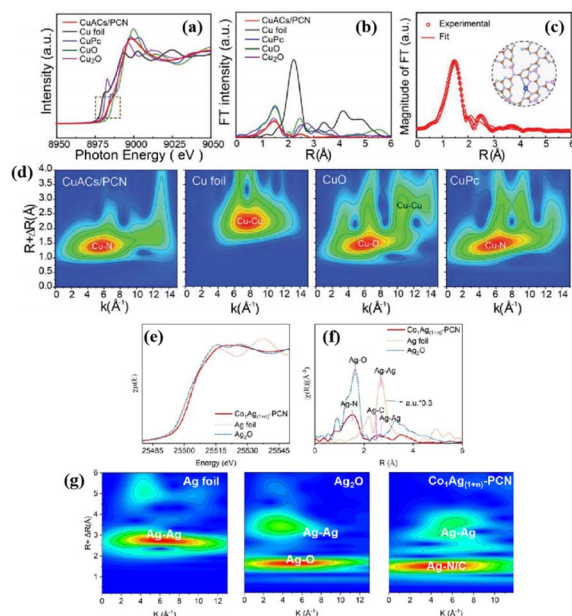
Fig. 13 (a) XANES and (b) EXAFS spectra of the Cu K-edge of CuACs/PCN, Cu foil, Cu_2O, CuO, and CuPc. (c) The EXAFS fitting curves of CuACs/PCN at R-space. (d) WT EXAFS of the Cu K-edge. These figures have been reproduced from ref. 85 with permission from Wiley-VCH, copyright 2022. Ag K-edge (e) XANES, (f) EXAFS, and (g) WT-EXAFS spectra of $Co_1Ag_{(1+n)}$-PCN. These figures have been reproduced from ref. 110 with permission from American Chemical Society, copyright 2023.

shell layer of Ag–N and the second shell layer of Ag–C, respectively. The presence of Ag–Ag coordination (2.6 Å) indicated that Ag existed in the form of single atoms and nanoparticles. The wavelet transform Ag K-edge EXAFS of $Co_1Ag_{(1+n)}$PCN showed a maximum peak around 4.7 Å, which was different from that of the Ag foil and Ag_2O, attributed to Ag–N/C coordination. Specifically, the EXAFS fitting of the shell coordination elucidated that the Ag atom was coordinated to 2.3 N atoms and 1.7C atoms, referred as the Ag–N_2C_2 site. Based on a similar analytical procedure, the existence of a Co–N_6–P configuration of the Co single atom in $Co_1Ag_{(1+n)}$PCN was also revealed.

4.4 Diffuse reflectance infrared Fourier-transformed spectroscopy (DRIFTS)

DRIFTS can be used to deduce the structure of the compound, reflecting the type of functional groups contained in the substance. Characterization of intermediates generated on the catalyst surface using in situ DRIFTS provides support for the reaction pathway revelation and MAS identification. In situ DRIFTS was used to probe the reaction intermediates in the CO_2 photoreduction of Er-doped $ZnIn_2S_4$.[86] Under dark conditions, Er-doped $ZnIn_2S_4$ exhibited distinct absorption peaks corresponding to monodentate carbonate (m-CO_3) and bidentate carbonate (b-CO_3), indicating the effective adsorption and activation of CO_2 and H_2O. Under light conditions, the peaks of *CHO (962 cm^{-1}), *OCH_3 (1043 cm^{-1}) and *COOH (1530 cm^{-1}) appeared in Er-$ZnIn_2S_4$, which were the key intermediates for the subsequent generation of CH_4. Both Er-$ZnIn_2S_4$ and pure

$ZnIn_2S_4$ showed absorption peaks for the *CH_2 group at 2856 and 2935 cm^{-1}, respectively, reflecting their tendency to generate CH_4. Compared to pure $ZnIn_2S_4$, the Er-$ZnIn_2S_4$ exhibited stronger b-CO_3 dissipation with stronger CO_2 reduction capacity. The spectrum of Er-$ZnIn_2S_4$ had additional *OCH_2 peaks between 1210–1240 cm^{-1}, reflecting different CO_2 reduction pathways between Er-$ZnIn_2S_4$ and $ZnIn_2S_4$ (Er-$ZnIn_2S_4$: CO_2 → *COOH → *CO → *CHO → *OCH_2 → *OCH_3 → CH_4; $ZnIn_2S_4$: CO_2 → *COOH → *CO → *CHO → *CH_2O → *CH → *CH_2 → *CH_3 → CH_4).

In situ DRIFTS identifies key intermediates of the C_{2+} product, contributing to the inference of C–C coupling processes. In this regard, crucial C_2 intermediates including COCO* (1374 and 1486 cm^{-1}) and COCOH* (1233 and 1574 cm^{-1}) were observed on the Au–CeO_2 nanocomposite, providing strong evidence that the Au–O–Ce sites drove the generation of C_2H_6 from the C–C coupling.[97] In addition, the peaks at 1367 and 1485 cm^{-1} appearing in the In_2O_3/InP heterojunction were related to OCCO*, a key intermediate in the generation of CH_3COOH.[120] The peak at 1332 cm^{-1} belonged to the C–H vibration of the hydrogenated intermediate after C–C coupling, and the peak at 1433 cm^{-1} belonged to the COO stretching vibration of CH_3COOH, further reflecting the generation of C_{2+}.

4.5 Raman

Raman spectroscopy identifies chemical bonds and functional groups. In situ Raman spectra can reveal the structural evolution of catalysts during catalytic reactions. For Vo-rich Zn_2GeO_4, CO_2 adsorption on Ge and Zn atoms gradually shifted the peak positions of the Zn–O–Ge stretching vibrations (∼730 cm^{-1}) and Zn–O–Ge bending vibrations (∼785 cm^{-1}) to higher wave numbers.[96] The Raman peak blue shift revealed the transfer of the electron cloud from the lattice oxygen to the metal atoms. The Zn–O–Ge stretching and Zn–O–Ge bending vibration peaks were again shifted to higher frequencies during CO_2 photoreduction, indicating that the electron cloud in the O 2p orbitals of the lattice oxygen was further transferred to the nearby Zn 4s or Ge 4s empty orbitals. This process provided electrons for the reduction of adsorbed CO_2 molecules and reaction intermediates. In situ Raman enables the real-time monitoring of the intermediate generation and conversion processes on the catalyst surface, revealing the reaction mechanism. In the in situ Raman spectrum, the peak before 500 cm^{-1} was related to the structural properties of r-In_2O_3/InP.[120] With increasing light duration, the peak at 887 cm^{-1} was designated as C–C–O stretching, reflecting the critical C–C coupling process for CH_3COOH generation. The C≡O stretching vibration of CO* (2909 cm^{-1}) further validated that the CO* coupling produced CH_3COOH.

4.6 Electrochemical analysis

Electrochemical analysis is widely used to reveal the kinetic processes of the migration and separation of photogenerated carriers in photocatalysis. Among them, transient photocurrent response and electrochemical impedance measurement (EIS)

are the most representative and widely used methods.[140–144] For example, the Cu–N$_4$ sites-anchored phosphorus-modulated carbon nitride (CuACs/PCN) exhibited the strongest photocurrent response relative to carbon nitride (CN), CuACs-anchored carbon nitride (CuACs/CN), and CuACs/PCNs with different P doping contents, reflecting its superior interfacial charge separation efficiency.[85] Moreover, EIS also demonstrated the lowest resistance of CuACs/PCN, thus confirming the efficient separation of photoexcited electron–hole pairs.

As another crucial feature, electrochemical analysis contributes to reveal the change of activation and reduction energy of CO$_2$ conversion. Kang's research group examined the Tafel plots of pure Cu, Cu/PVP and Cu/rGO/PVP/Nafion composite electrodes to estimate the reaction overpotentials of the samples.[145] The overpotentials of Cu/PVP (6.16 kJ mol^{-1}) and Cu/rGO/PVP/Nafion (9.00 kJ mol^{-1}) electrodes were significantly lower than those of the pure Cu electrode, revealing a decrease in the CO$_2$ reduction energy.

In addition, the Mott–Schottky measurement can be used to specify the semiconductor type and determine the valence band maximum (VBM) and conduction band minimum (CBM) potentials. For example, according to the results of the Mott–Schottky test, the Zr/Ti bimetallic oxide solid solution integrated with Au nanoparticles (Au/TZO) exhibited the characteristics of n-type semiconductors.[131] As the CBM of Au/TZO was estimated as −0.80 V with respect to a normal hydrogen electrode (NHE), the photocatalytic conversion of CO$_2$ to CO (−0.53 vs. NHE), CH$_4$ (−0.24 vs. NHE), C$_2$H$_4$ (−0.34 vs. NHE) and C$_2$H$_6$ (−0.27 vs. NHE) was thermodynamically feasible over Au/TZO. It is also worth mentioning that the electrochemical active surface area (ECSA) can be used to reveal the number of catalytically active sites. A larger ECSA indicates more active sites, which is more favorable for photocatalytic CO$_2$ conversion.[146]

4.7 Theoretical calculations

Theoretical calculations can be used to obtain the atomic and electronic structures of the MAS, the adsorption strength of the intermediates, and the optimal reaction path.

Electronic property analysis can infer underlying factors affecting the catalytic activity. The d-band centers of Cu in Cu$_1$N$_3$@P(1)CN, Cu$_1$N$_3$@CN, and Cu$_1$P$_3$@PCN were determined to be −1.24 eV, −1.46 eV, and 11.60 eV, respectively, by partial density of states analysis, which depended on the local coordination environment of Cu.[87] As the d-band center of Cu approached the Fermi energy level, the catalytic activity for the COOH* formation became higher. It is worth mentioning that the overlap between Cu 3d and P 3p in Cu$_1$N$_3$@P(1)CN was more pronounced than the overlap of Cu 3d with C 2p at the same corner position in Cu$_1$N$_3$@CN. This reflected the more pronounced orbital and electronic interactions of Cu and P in Cu$_1$N$_3$@P(1)CN than that of Cu and C in Cu$_1$N$_3$@CN, which moved the d-band center of Cu$_1$N$_3$@PCN closer to the Fermi energy level. Charge density difference analysis further demonstrated that the electronic interaction between Cu and COOH* in Cu$_1$N$_3$@P(1)CN was the strongest relative to Cu$_1$N$_3$@CN and Cu$_1$P$_3$@PCN, prompting a large number of

electrons to be transferred from the Cu center to COOH* in Cu$_1$N$_3$@P(1)CN, benefiting CO$_2$ activation.

Theoretical calculations provide insight into the mechanism of the photocatalytic CO$_2$ reduction reaction. From the free energy analysis, the introduction of Ag single atoms on hollow porous polygonal C$_3$N$_4$ nanotubes (Ag$_1$@PCNT) significantly enhanced the adsorption of *CO$_2$ and weakened the adsorption of *H, suggesting that Ag$_1$@PCNT was more favorable for CO$_2$ conversion than for hydrogen production.[88] The COOH* formation energy (the rate-limiting step) of Ag$_1$@PCNT was lower than that of C$_3$N$_4$ nanotubes. This suggests that the strong interaction of the Ag–N$_3$ coordination with *COOH stabilized the *COOH intermediate and reduced the barrier for CO$_2$ photoreduction (Fig. 14a and b). In addition, the generation of CO molecules by desorption of *CO groups on the surface of Ag$_1$@PCNT had a smaller Gibbs free energy than the protonation of *CO into *CHO, which contributed to the highly selective generation of CO.

Theoretical calculations can reveal the specific processes involved in the generation of C$_{2+}$ products, especially for C–C coupling. Calculation of the Gibbs free energy diagrams for CO$_2$ photoreduction on In and/or Cu-anchored poly-CN (InCu/poly-CN, Cu/poly-CN, and In/poly-CN) (Fig. 14c) revealed that the formation of *COOH was a rate-determining step on InCu/poly-CN (ΔG = +1.20 eV) and In/poly-CN (ΔG = +1.86 eV), while the generation of *COCH$_2$OH was a rate-determining step on Cu/poly-CN (ΔG = +1.98 eV).[98] On InCu/poly-CN, *CO underwent a dimerization reaction (ΔG = 0.45 eV) and a subsequent hydrogenation–electron addition process to ultimately generate CH$_3$CH$_2$OH. In the Cu/poly-CN system, *CO was also coupled to form *COCO, but its Gibbs free energy was higher than that of the InCu/poly-CN. Furthermore, the process from *COCHOH to *COCH$_2$OH in Cu/poly-CN was endothermic with the highest gain (ΔG = +1.98 eV), resulting in lower CH$_3$CH$_2$OH yields for Cu/poly-CN relative to InCu/poly-CN. However, the *CO
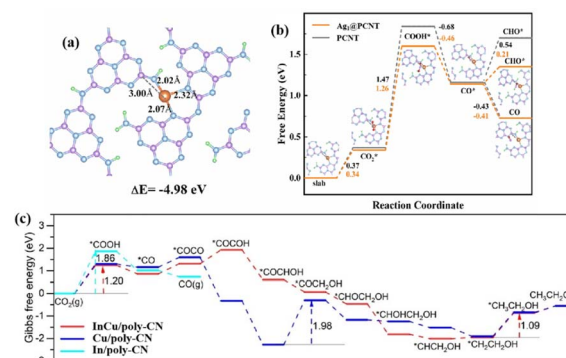

Fig. 14 (a) Structure of Ag$_1$@PCNT. (b) Gibbs free energies of the CO$_2$ photoreduction pathways by DFT calculations over the Ag$_1$@PCNT (Ag sites) and PCNT surfaces. Atom key: N (blue), C (purple), H (green), and Ag (orange). These figures have been reproduced from ref. 88 with permission from Wiley-VCH, copyright 2023. Gibbs free energy diagrams and CO$_2$-to-ethanol photoreduction pathways on InCu/poly-CN, Cu/poly-CN, and In/poly-CN (c). This figure has been reproduced from ref. 98 with permission from Wiley-VCH, copyright 2022.

intermediates on In/poly-CN preferred desorption as CO products (exothermic) rather than C–C coupling, resulting in a poor CH_3CH_2OH yield on In/poly-CN.

5 Conclusion and perspectives

The photocatalysts containing MAS have been proved as efficient systems for converting incident solar energy into chemical fuel. In this review, typical photocatalytic materials containing MAS have been briefly introduced with clear examples. Then, the different roles of MAS in various forms in the photocatalytic CO_2 reduction from the perspective of principles and applications are discussed in detail, greatly accelerating the surface charge separation/transfer, and enhancing the adsorption and activation of CO_2. Finally, advanced characterization techniques and theoretical calculation for revealing the function played by MAS in CO_2 photoreduction are presented. Although considerable progress has been made in MAS-containing photocatalytic systems, there are still great challenges in practical applications that need to be further explored.

(1) The complexity of the preparation process and the difficulty of achieving uniform high-volume production are the major drawbacks of MAS-containing catalysts. In addition, the exposed MAS are susceptible to oxidation, resulting in performance degradation. Therefore, effective technologies should be continuously developed for the large-scale production of MAS-containing photocatalysts with stable and controllable surface states. Elaborate design strategies to improve the catalyst stability (e.g., surface encapsulation and ligand grafting) need to be further explored. Continuous optimization of existing synthesis methods is an effective and viable solution.

(2) Although photocatalysts containing MAS have shown great potential in artificial photosynthesis, their performance is still unsatisfactory for practical production. Particularly, photocatalytic CO_2 conversion involves a variety of intermediates and products, making it difficult to regulate the selectivity of the target product. For photocatalytic systems with MAS, the interactions of reactants and intermediates with the MAS affect the activation and conversion of CO_2, as well as C–C coupling. Defect design, doping, construction of heterostructures, and introduction of co-catalysts have become widely used strategies to enhance the CO_2 photoreduction performance. However, there is still a need to continuously explore effective and novel strategies to improve the performance for real-world production, which remains elusive at the present stage.

(3) Accurate characterization and in-depth understanding of the mechanism of MAS in photocatalysis still face great challenges. It is crucial to carefully reveal the coordination environments of the MAS and its changes during the photocatalytic reaction. Specifically, the working mechanism of MAS in photocatalysis can be explored in-depth by advanced *in situ* characterisation techniques and accurate theoretical calculations, which guide the rational design and regulation of photocatalysts. Therefore, there is a need for the continuous development of highly sophisticated characterisation techniques, and theoretical computational models close to the actual reaction processes.

(4) In the face of the explosion of research data, the traditional research method of relying on pre-investigation to identify scientific problems has become overwhelming. This approach is costly, time-consuming, and increasingly difficult to meet the research needs of modern materials science. Nowadays, machine learning is changing the traditional research paradigm and bringing new opportunities for the development of related technologies and industrial upgrading. Combining machine learning techniques with the design of photocatalytic systems to rapidly mine effective information from a large amount of data is conducive to the construction of novel materials and the excavation of reaction mechanisms. Specifically, machine learning techniques are becoming a powerful tool for scientific research in the design and construction of photocatalysts, as well as in the prediction of physicochemical properties and mechanisms.

In summary, through continuous exploration and in-depth research, it is found that photocatalytic CO_2 reduction technology is expected to realize the establishment of a resource-saving and environmentally-friendly energy system, and improve human life in the near future.

Data availability

No primary research results, software or code have been included and no new data were generated or analysed as part of this review.

Author contributions

All authors participated in this review work. W. Gao, Y. Yang, and Y. Zhou conceived the structure of this perspective. W. Gao, H. N. Li, and J. Q. Hu prepared the draft. Y. J. Xiong, J. H. Ye, and Z. G. Zou reviewed and refined the manuscript.

Conflicts of interest

There are no conflicts to declare.

Acknowledgements

References

1 C. Y. Feng, Z. P. Wu, K. W. Huang, J. H. Ye and H. B. Zhang, *Adv. Mater.*, 2022, **34**, 202200180.

2 E. Gong, S. Ali, C. B. Hiragond, H. S. Kim, N. S. Powar, D. Kim, H. Kim and S. I. In, *Energy Environ. Sci.*, 2022, **15**, 880–937.

3 H. W. Lin, S. N. Luo, H. B. Zhang and J. H. Ye, *Joule*, 2022, **6**, 294–314.

4 R. Ham, C. J. Nielsen, S. Pullen and J. N. H. Reek, *Chem. Rev.*, 2023, **123**, 5225–5261.

5 X. J. Liu, T. Q. Chen, Y. H. Xue, J. C. Fan, S. L. Shen, M. Hossain, M. A. Amin, L. K. Pan, X. T. Xu and Y. Yamauchi, *Coord. Chem. Rev.*, 2022, **459**, 214440.

6 B. C. Qiu, M. M. Du, Y. X. Ma, Q. H. Zhu, M. Y. Xing and J. L. Zhang, *Energy Environ. Sci.*, 2021, **14**, 5260–5288.

7 K. H. Chen, X. W. Wang, Q. Y. Li, Y. N. Feng, F. F. Chen and Y. Yu, *Chem. Eng. J.*, 2021, **418**, 129476.

8 L. Cheng, D. N. Zhang, Y. L. Liao, J. J. Fan and Q. J. Xiang, *Chin. J. Catal.*, 2021, **42**, 131–140.

9 J. W. Jiang, X. F. Wang, Q. J. Xu, Z. Y. Mei, L. Y. Duan and H. Guo, *Appl. Catal., B*, 2022, **316**, 121679.

10 G. H. Li, Y. Y. Sun, Q. M. Zhang, Z. Gao, W. Sun and X. X. Zhou, *Chem. Eng. J.*, 2021, **410**, 128397.

11 J. X. Liang, H. Yu, J. J. Shi, B. Li, L. X. Wu and M. Wang, *Adv. Mater.*, 2023, **35**, 202209814.

12 W. B. Jiang, H. Y. Loh, B. Q. L. Low, H. J. Zhu, J. X. Low, J. Z. X. Heng, K. Y. Tang, Z. B. Li, X. J. Loh, E. Y. Ye and Y. J. Xiong, *Appl. Catal., B*, 2023, **321**, 122079.

13 S. M. Mao, J. W. Shi, G. T. Sun, D. D. Ma, C. He, Z. X. Pu, K. L. Song and Y. H. Cheng, *Appl. Catal., B*, 2021, **282**, 119550.

14 Z. Y. Dong, L. Zhang, J. Gong and Q. Zhao, *Chem. Eng. J.*, 2021, **403**, 126383.

15 S. K. Yin, L. L. Sun, Y. J. Zhou, X. Li, J. Z. Li, X. H. Song, P. W. Huo, H. Q. Wang and Y. S. Yan, *Chem. Eng. J.*, 2021, **406**, 126776.

16 J. Zhang, L. T. Li, M. Du, Y. Cui, Y. H. Li, W. Yan, H. J. Huang, X. A. Li and X. B. Zhu, *Small*, 2023, **19**, 202300402.

17 H. H. Ou, S. B. Ning, P. Zhu, S. H. Chen, A. Han, Q. Kang, Z. F. Hu, J. H. Ye, D. S. Wang and Y. D. Li, *Angew. Chem., Int. Ed.*, 2022, **61**, 202206579.

18 J. P. Sheng, Y. He, J. Y. Li, C. W. Yuan, H. W. Huang, S. Y. Wang, Y. J. Sun, Z. M. Wang and F. Dong, *ACS Nano*, 2020, **14**, 13103–13114.

19 N. Podrojková, V. Sans, A. Orinak and R. Orinaková, *ChemCatChem*, 2020, **12**, 1802–1825.

20 J. Wang, W. B. Zhu, F. Y. Meng, G. Y. Bai, Q. F. Zhang and X. W. Lan, *ACS Catal.*, 2023, **13**, 4316–4329.

21 F. F. Chen, L. H. Zhou, C. Peng, D. T. Zhang, L. Y. Li, D. F. Xue and Y. Yu, *Appl. Catal., B*, 2023, **331**, 122689.

22 J. Di, C. Chen, C. Zhu, P. Song, M. L. Duan, J. Xiong, R. Long, M. Z. Xu, L. X. Kang, S. S. Guo, S. M. Chen, H. L. Chen, Z. Chi, Y. X. Weng, H. M. Li, L. Song, M. H. Wu, Q. Y. Yan, S. Z. Li and Z. Liu, *Nano Energy*, 2021, **79**, 105429.

23 J. Li, B. J. Huang, Q. Guo, S. Guo, Z. K. Peng, J. Liu, Q. Y. Tian, Y. P. Yang, Q. Xu, Z. Y. Liu and B. Liu, *Appl. Catal., B*, 2021, **284**, 119733.

24 H. W. Guo, S. P. Wan, Y. A. Wang, W. H. Ma, Q. Zhong and J. Ding, *Chem. Eng. J.*, 2021, **412**, 128646.

25 J. Li, W. F. Pan, Q. Y. Liu, Z. Q. Chen, Z. J. Chen, X. Z. Feng and H. Chen, *J. Am. Chem. Soc.*, 2021, **143**, 6551–6559.

26 Y. Y. Wang, H. L. Huang, Z. Z. Zhang, C. Wang, Y. Y. Yang, Q. Li and D. S. Xu, *Appl. Catal., B*, 2021, **282**, 119570.

27 L. Cheng, P. Zhang, Q. Y. Wen, J. J. Fan and Q. J. Xiang, *Chin. J. Catal.*, 2022, **43**, 451–460.

28 Q. J. Wu, J. Liang, Y. B. Huang and R. Cao, *Acc. Chem. Res.*, 2022, **55**, 2978–2997.

29 F. Guo, R. X. Li, S. Z. Yang, X. Y. Zhang, H. J. Yu, J. J. Urban and W. Y. Sun, *Angew. Chem., Int. Ed.*, 2023, **62**, 202216232.

30 W. Wang, C. Y. Deng, S. J. Xie, Y. F. Li, W. Y. Zhang, H. Sheng, C. C. Chen and J. C. Zhao, *J. Am. Chem. Soc.*, 2021, **143**, 2984–2993.

31 G. Wang, Z. Chen, T. Wang, D. S. Wang and J. J. Mao, *Angew. Chem., Int. Ed.*, 2022, **61**, 202210789.

32 X. H. Yang, X. W. Lan, Y. Z. Zhang, H. S. Li and G. Y. Bai, *Appl. Catal., B*, 2023, **325**, 122393.

33 H. Yu, C. Sun, Y. Xuan, K. Zhang and K. Chang, *Chem. Eng. J.*, 2022, **430**, 132940.

34 S. P. Wan, M. Ou, Q. Zhong and X. M. Wang, *Chem. Eng. J.*, 2019, **358**, 1287–1295.

35 S. L. Wang, M. Xu, T. Y. Peng, C. X. Zhang, T. Li, I. Hussain, J. Y. Wang and B. E. Tan, *Nat. Commun.*, 2019, **10**, 08651.

36 G. Wang, R. Huang, J. W. Zhang, J. J. Mao, D. S. Wang and Y. D. Li, *Adv. Mater.*, 2021, **33**, 202105904.

37 X. L. Zhuang, S. T. Zhang, Y. J. Tang, F. Yu, Z. M. Li and H. Pang, *Coord. Chem. Rev.*, 2023, **490**, 215208.

38 T. Wang, L. Chen, C. Chen, M. T. Huang, Y. J. Huang, S. J. Liu and B. X. Li, *ACS Nano*, 2022, **16**, 2306–2318.

39 P. Y. Li, L. Liu, W. J. An, H. Wang, H. X. Guo, Y. H. Liang and W. Q. Cui, *Appl. Catal., B*, 2020, **266**, 118618.

40 Y. J. Liang, X. Wu, X. Y. Liu, C. H. Li and S. W. Liu, *Appl. Catal., B*, 2022, **304**, 120978.

41 S. J. Xie, W. C. Ma, X. J. Wu, H. K. Zhang, Q. H. Zhang, Y. D. Wang and Y. Wang, *Energy Environ. Sci.*, 2021, **14**, 37–89.

42 Y. N. Teja and M. Sakar, *Small*, 2023, **19**, 202303980.

43 W. G. Tu, Y. Zhou, Q. Liu, Z. P. Tian, J. Gao, X. Y. Chen, H. T. Zhang, J. G. Liu and Z. G. Zou, *Adv. Funct. Mater.*, 2012, **22**, 1215–1221.

44 X. H. Yan, J. J. Zhang, G. Z. Hao, W. Jiang and J. Di, *Small*, 2024, **20**, 202306742.

45 Y. M. Zhou, Q. X. Zhang, X. L. Shi, Q. Song, C. J. Zhou and D. L. Jiang, *J. Colloid Interface Sci.*, 2022, **608**, 2809–2819.

46 Y. Shen, C. J. Ren, L. R. Zheng, X. Y. Xu, R. Long, W. Q. Zhang, Y. Yang, Y. C. Zhang, Y. F. Yao, H. Q. Chi, J. L. Wang, Q. Shen, Y. J. Xiong, Z. G. Zou and Y. Zhou, *Nat. Commun.*, 2023, **14**, 1117.

47 L. J. Xiong, Y. J. Hu, Y. Wang, W. Dong, X. Y. Zhang, K. Zhang, T. Y. Wang, J. Y. Shen and Y. Yang, *Appl. Catal., B*, 2024, **340**, 123263.

48 H. Pang, X. G. Meng, H. Song, W. Zhou, G. L. Yang, H. W. Zhang, Y. Izumi, T. Takei, W. Jewasuwan, N. Fukata and J. H. Ye, *Appl. Catal., B*, 2019, **244**, 1013–1020.

49 X. D. Zhang, D. Kim and L. Y. S. Lee, *ACS Appl. Energy Mater.*, 2021, **4**, 2586–2592.

50 C. Hu, H. Y. Sun, X. M. Jia, H. L. Lin, J. Cao and S. F. Chen, *ChemPhotoChem*, 2022, **6**, 202200150.

51 Y. Q. He, C. L. Chen, Y. X. Liu, Y. L. Yang, C. G. Li, Z. Shi, Y. Han and S. H. Feng, *Nano Lett.*, 2022, **22**, 4970–4978.

52 S. Si, H. Shou, Y. Mao, X. Bao, G. Zhai, K. Song, Z. Wang, P. Wang, Y. Liu, Z. Zheng, Y. Dai, L. Song, B. Huang and H. Cheng, *Angew. Chem., Int. Ed.*, 2022, **61**, e202209446.

53 Y. Q. He, H. Rao, K. P. Song, J. X. Li, Y. Yu, Y. Lou, C. G. Li, Y. Han, Z. Shi and S. H. Feng, *Adv. Funct. Mater.*, 2019, **29**, 201905153.

54 W. Gao, S. Li, H. C. He, X. N. Li, Z. X. Cheng, Y. Yang, J. L. Wang, Q. Shen, X. Y. Wang, Y. J. Xiong, Y. Zhou and Z. G. Zou, *Nat. Commun.*, 2021, **12**, 4747.

55 W. Gao, L. Shi, W. Hou, C. Ding, Q. Liu, R. Long, H. Chi, Y. Zhang, X. Xu, X. Ma, Z. Tang, Y. Yang, X. Wang, Q. Shen, Y. Xiong, J. Wang, Z. Zou and Y. Zhou, *Angew. Chem., Int. Ed.*, 2024, **63**, e202317852.

56 X. Y. Xiong, Y. F. Zhao, R. Shi, W. J. Yin, Y. X. Zhao, G. I. N. Waterhouse and T. R. Zhang, *Sci. Bull.*, 2020, **65**, 987–994.

57 S. Yu, L. Tan, S. Bai, C. J. Ning, G. H. Liu, H. J. Wang, B. Liu, Y. F. Zhao and Y. F. Song, *Small*, 2022, **18**, 202202334.

58 Y. L. Li, Q. Zhao, X. J. Liu, Y. Liu, Y. J. Hao, X. J. Wang, X. Y. Liu, D. Hildebrandt, F. Y. Li and F. T. Li, *Small Struct.*, 2023, **4**, 202300177.

59 Z. H. Wei, S. J. Song, H. F. Gu, Y. Q. Li, Q. Sun, N. Ding, H. Tang, L. R. Zheng, S. H. Liu, Z. X. Li, W. X. Chen, S. H. Li and S. P. Pang, *Adv. Sci.*, 2023, **10**, 202303206.

60 K. Sun, Y. Qian and H. L. Jiang, *Angew. Chem., Int. Ed.*, 2023, **62**, e202217565.

61 J. X. Wang, K. Sun, D. A. Wang, X. W. Niu, Z. Y. Lin, S. Y. Wang, W. J. Yang, J. R. Huang and H. L. Jiang, *ACS Catal.*, 2023, **13**, 8760–8769.

62 M. R. Zhang, D. Zhang, X. Jing, B. J. Xu and C. Y. Duan, *Angew. Chem., Int. Ed.*, 2024, **63**, 202402755.

63 Y. Z. Zhang, L. L. Cao, G. Y. Bai and X. W. Lan, *Small*, 2023, **19**, 202300035.

64 W. G. Tu, Y. Q. Yang, C. P. Chen, T. H. Zhou, T. H. Li, H. J. Wang, S. Y. Wu, Y. Zhou, D. O'Hare, Z. G. Zou and R. Xu, *Small Struct.*, 2023, **4**, 202200233.

65 Q. Zhang, S. Q. Gao, Y. Y. Guo, H. Y. Wang, J. S. Wei, X. F. Su, H. C. Zhang, Z. M. Liu and J. J. Wang, *Nat. Commun.*, 2023, **14**, 1147.

66 M. P. Kou, W. Liu, Y. Y. Wang, J. D. Huang, Y. L. Chen, Y. Zhou, Y. Chen, M. Z. Ma, K. Lei, H. Q. Xie, P. K. Wong and L. Q. Ye, *Appl. Catal., B*, 2021, **291**, 120146.

67 P. Chen, B. Lei, X. A. Dong, H. Wang, J. P. Sheng, W. Cui, J. Y. Li, Y. J. Sun, Z. M. Wang and F. Dong, *ACS Nano*, 2020, **14**, 15841–15852.

68 K. Wang, M. Cheng, F. J. Xia, N. Cao, F. X. Zhang, W. K. Ni, X. Y. Yue, K. P. Yan, Y. He, Y. Shi, W. X. Dai and P. F. Xie, *Small*, 2023, **19**, 202207581.

69 L. Cheng, X. Y. Yue, L. X. Wang, D. N. Zhang, P. Zhang, J. J. Fan and Q. J. Xiang, *Adv. Mater.*, 2021, **33**, 202105135.

70 L. Zeng, J. W. Chen, L. X. Zhong, W. L. Zhen, Y. Y. Tay, S. Z. Li, Y. G. Wang, L. M. Huang and C. Xue, *Appl. Catal., B*, 2022, **307**, 121154.

71 W. Xia and F. Wang, *Mol. Catal.*, 2023, **535**, 112884.

72 Y. C. Wang, J. H. Zhang, W. Yang, W. X. Tao, K. Y. Tao, J. H. Deng, W. J. Shi, D. C. Zhong and T. B. Lu, *Chin. J. Chem.*, 2023, **41**, 3305–3310.

73 L. Yuan, L. Zhang, X. X. Li, J. Liu, J. J. Liu, L. Z. Dong, D. S. Li, S. L. Li and Y. Q. Lan, *Chin. Chem. Lett.*, 2023, **34**, 039.

74 R. Xu, D. H. Si, S. S. Zhao, Q. J. Wu, X. S. Wang, T. F. Liu, H. Zhao, R. Cao and Y. B. Huang, *J. Am. Chem. Soc.*, 2023, **145**, 8261–8270.

75 J. Q. Ning, W. Chen, Q. Niu, L. Y. Li and Y. Yu, *ChemSusChem*, 2024, DOI: **10.1002/cssc.202301963**.

76 S. J. Liang, X. H. Zhong, Z. Q. Zhong, H. Deng and W. Y. Wong, *Appl. Catal., B*, 2023, **337**, 122958.

77 H. B. Yin, F. Dong, D. S. Wang and J. H. Li, *ACS Catal.*, 2022, **12**, 14096–14105.

78 C. Y. Shen, X. Y. Meng, R. Zou, K. H. Sun, Q. L. Wu, Y. X. Pan and C. J. Liu, *Angew. Chem., Int. Ed.*, 2024, **63**, 202402369.

79 Q. Y. Wang, Y. D. Zhang, M. X. Lin, H. W. Wang, Y. Bai, C. Y. Liu, J. L. Lu, Q. Q. Luo, G. M. Wang, H. L. Jiang, T. Yao and X. S. Zheng, *Adv. Energy Mater.*, 2023, **13**, 202302692.

80 F. Guo, R. X. Li, S. Yang, X. Y. Zhang, H. Yu, J. J. Urban and W. Y. Sun, *Angew. Chem., Int. Ed.*, 2023, **62**, 202216232.

81 H. Shi, Y. Liang, J. Hou, H. Wang, Z. Jia, J. Wu, F. Song, H. Yang and X. Guo, *Angew. Chem., Int. Ed.*, 2024, **63**, e202404884.

82 Y. Y. Mao, M. H. Zhang, S. H. Si, G. Y. Zhai, X. L. Bao, K. P. Song, L. R. Zheng, Y. Y. Liu, Z. Y. Wang, Z. K. Zheng, P. Wang, Y. Dai, H. F. Cheng and B. B. Huang, *ACS Catal.*, 2023, **13**, 8362–8371.

83 C. Y. Feng, T. T. Bo, P. Maity, S. W. Zuo, W. Zhou, K. W. Huang, O. F. Mohammed and H. B. Zhang, *Adv. Funct. Mater.*, 2023, **34**, 202309761.

84 C. Ding, X. X. Lu, B. Tao, L. Q. Yang, X. Y. Xu, L. Q. Tang, H. Q. Chi, Y. Yang, D. M. Meira, L. Wang, X. Zhu, S. Li, Y. Zhou and Z. G. Zou, *Adv. Funct. Mater.*, 2023, **33**, 202302824.

85 W. K. Xie, K. J. Li, X. H. Liu, X. Zhang and H. W. Huang, *Adv. Mater.*, 2023, **35**, 202208132.

86 F. H. Zhou, Y. L. Zhang, J. Wu, W. Yang, X. Fang, T. Jia, Y. Ling, P. He, Q. Z. Liu and J. Lin, *Appl. Catal., B*, 2024, **341**, 123347.

87 X. Sun, L. Sun, G. Li, Y. Tuo, C. Ye, J. Yang, J. Low, X. Yu, J. H. Bitter, Y. Lei, D. Wang and Y. Li, *Angew. Chem., Int. Ed.*, 2022, **61**, 202207677.

88 S. Hu, P. Z. Qiao, X. L. Yi, Y. M. Lei, H. L. Hu, J. H. Ye and D. F. Wang, *Angew. Chem., Int. Ed.*, 2023, **62**, 202304585.

89 M. Z. Ma, Z. Huang, L. A. Li, W. D. Zhang, R. Guo, R. Y. Zhang, W. Fa, C. Q. Han, Y. H. Cao, S. Yu and Y. Zhou, *Appl. Catal., B*, 2023, **330**, 122626.

90 J. Zhou, J. Li, L. Kan, L. Zhang, Q. Huang, Y. Yan, Y. F. Chen, J. Liu, S. L. Li and Y. Q. Lan, *Nat. Commun.*, 2022, **13**, 32449.

91 M. Zhou, Z. Q. Wang, A. H. Mei, Z. F. Yang, W. Chen, S. Y. Ou, S. Y. Wang, K. Q. Chen, P. Reiss, K. Qi, J. Y. Ma and Y. L. Liu, *Nat. Commun.*, 2023, **14**, 2473.

92 X. D. Li, Y. F. Sun, J. Q. Xu, Y. J. Shao, J. Wu, X. L. Xu, Y. Pan, H. X. Ju, J. F. Zhu and Y. Xie, *Nat. Energy*, 2019, **4**, 690–699.

93 S. M. Deng, R. H. Wang, X. Z. Feng, R. J. Zheng, S. K. Gong, X. H. Chen, Y. Z. Shangguan, L. L. Deng, H. Tang, H. Dai, L. L. Duan, C. Y. Liu, Y. Pan and H. Chen, *Angew. Chem., Int. Ed.*, 2023, **62**, 202309625.

94 C. Chen, L. Chen, Y. G. Hu, K. Yan, T. Wang, Y. J. Huang, C. Gao, J. J. Mao, S. J. Liu and B. X. Li, *J. Energy Chem.*, 2023, **86**, 599–608.

95 Y. Z. Zhang, B. Johannessen, P. Zhang, J. L. Gong, J. R. Ran and S. Z. Qiao, *Adv. Mater.*, 2023, **35**, 202306923.

96 J. C. Zhu, W. W. Shao, X. D. Li, X. C. Jiao, J. F. Zhu, Y. F. Sun and Y. Xie, *J. Am. Chem. Soc.*, 2021, **143**, 18233–18241.

97 J. X. Ji, R. R. Li, H. Zhang, Y. N. Duan, Q. Liu, H. Z. Wang and Z. R. Shen, *Appl. Catal., B*, 2023, **321**, 122020.

98 H. Shi, H. Wang, Y. Zhou, J. Li, P. Zhai, X. Li, G. G. Gurzadyan, J. Hou, H. Yang and X. Guo, *Angew. Chem., Int. Ed.*, 2022, **61**, 202208904.

99 B. Liu, M. Cheng, C. Zhang, Y. Si, J. Zhou, Y. Ren, J. Guan, L. Duan, M. Liu, D. Jing and N. Li, *Appl. Catal., B*, 2024, **357**, 124263.

100 X. F. Shang, G. J. Li, R. A. Wang, T. Xie, J. Ding and Q. Zhong, *Chem. Eng. J.*, 2023, **456**, 140805.

101 G. R. Jia, M. Z. Sun, Y. Wang, Y. B. Shi, L. Z. Zhang, X. Q. Cui, B. L. Huang and J. C. Yu, *Adv. Funct. Mater.*, 2022, **32**, 202206817.

102 J. L. Yin, D. Y. Li, C. Sun, Y. L. Jiang, Y. K. Li and H. H. Fei, *Adv. Mater.*, 2024, **36**, 2403651.

103 W. W. Wang, S. J. Song, P. Wang, M. He, Z. Fang, X. L. Yuan, H. Li, C. Y. Li, X. Wang, Y. C. Wei, W. Y. Song, H. Xu and Z. X. Li, *ACS Catal.*, 2023, **13**, 4597–4610.

104 S. J. Xie, Y. F. Li, B. Sheng, W. Y. Zhang, W. Wang, C. C. Chen, J. K. Li, H. Sheng and J. C. Zhao, *Appl. Catal., B*, 2022, **310**, 121320.

105 Z. F. Ma, X. Liu, X. S. Wang, Z. G. Luo, W. R. Li, Y. H. Nie, L. Pei, Q. A. Mao, X. Wen and J. S. Zhong, *Chem. Eng. J.*, 2023, **468**, 143569.

106 Y. Y. Duan, Y. Wang, W. X. Zhang, J. W. Zhang, C. G. Ban, D. M. Yu, K. Zhou, J. J. Tang, X. Zhang, X. D. Han, L. Y. Gan, X. P. Tao and X. Y. Zhou, *Adv. Funct. Mater.*, 2023, **33**, 202301729.

107 J. Y. Wang, C. Yang, L. Mao, X. Y. Cai, Z. K. Geng, H. Y. Zhang, J. Y. Zhang, X. Tan, J. H. Ye and T. Yu, *Adv. Funct. Mater.*, 2023, **33**, 202213901.

108 X. Shi, W. D. Dai, X. A. Dong, Q. Ren, J. P. Sheng and F. Dong, *Appl. Catal., B*, 2023, **339**, 123147.

109 W. G. Pan, C. F. Li, Z. R. Zhang, T. Wu and R. T. Guo, *Appl. Catal., B*, 2024, **343**, 123492.

110 A. X. Deng, E. Zhao, Q. Li, Y. Sun, Y. Z. Liu, S. G. Yang, H. He, Y. Xu, W. Zhao, H. O. Song, Z. Xu and Z. P. Chen, *ACS Nano*, 2023, **17**, 11869–11881.

111 M. H. Zhang, Y. Y. Mao, X. L. Bao, P. Wang, Y. Y. Liu, Z. K. Zheng, H. F. Cheng, Y. Dai, Z. Y. Wang and B. B. Huang, *ACS Catal.*, 2024, **14**, 5275–5285.

112 P. G. Liu, Z. X. Huang, X. P. Gao, X. Hong, J. F. Zhu, G. M. Wang, Y. E. Wu, J. Zeng and X. S. Zheng, *Adv. Mater.*, 2022, **34**, 202200057.

113 X. H. Li, F. H. Li, S. L. Tong, Y. J. Cao, Y. W. Jiang, Z. M. Wang, W. Lu, J. Wu, T. Zhou, J. Lin and Y. S. Liu, *J. Alloys Compd.*, 2024, **984**, 173986.

114 X. T. Wang, Z. Z. Wang, Y. Li, J. T. Wang and G. K. Zhang, *Appl. Catal., B*, 2022, **319**, 121895.

115 Y. Zhang, F. Y. Guo, K. K. Wang, J. Di, B. K. Min, H. Y. Zhu, H. L. Chen, Y. X. Weng, J. Y. Dai, Y. B. She, J. X. Xia and H. M. Li, *Chem. Eng. J.*, 2023, **465**, 142663.

116 G. Wang, Y. Wu, Z. Li, Z. Lou, Q. Chen, Y. Li, D. Wang and J. Mao, *Angew. Chem., Int. Ed.*, 2023, **62**, e202218460.

117 Z. W. Zhao, Z. L. Wang, J. F. Zhang, C. F. Shao, K. Dai, K. Fan and C. H. Liang, *Adv. Funct. Mater.*, 2023, **33**, 202214470.

118 H. A. E. Omr, R. Putikam, S. P. Feng, M. C. Lin and H. Lee, *Appl. Catal., B*, 2023, **339**, 123103.

119 C. J. Ning, J. R. Yang, S. Bai, G. B. Chen, G. H. Liu, T. Y. Shen, L. R. Zheng, S. M. Xu, X. G. Kong, B. Liu, Y. F. Zhao and Y. F. Song, *Adv. Funct. Mater.*, 2023, **33**, 202300365.

120 S. Q. Gong, Y. L. Niu, X. Liu, C. Xu, C. C. Chen, T. J. Meyer and Z. F. Chen, *ACS Nano*, 2023, **17**, 4922–4932.

121 Y. Zhao, Z. D. Han, G. Y. Gao, W. Y. Zhang, Y. Qu, H. Y. Zhu, P. F. Zhu and G. F. Wang, *Adv. Funct. Mater.*, 2021, **31**, 202104976.

122 W. L. Dai, P. Wang, J. F. Long, Y. Xu, M. Zhang, L. X. Yang, J. P. Zou, X. B. Luo and S. L. Luo, *ACS Catal.*, 2023, **13**, 2513–2522.

123 H. B. Zhao, J. N. Huang, Q. Qin, H. Y. Chen and D. B. Kuang, *Small*, 2023, **19**, 202302022.

124 M. L. Guan, N. Lu, X. Zhang, Q. W. Wang, J. Bao, G. Y. Chen, H. Yu, H. M. Li, J. X. Xia and X. Z. Gong, *Carbon Energy*, 2023, **6**, e420.

125 H. J. Lu, N. Uddin, Z. H. Sun, Z. B. Chen, Z. Mahfoud, Y. L. Wu, A. A. Wibowo, Z. C. Su, X. M. Yin, C. S. Tang, X. Z. Liao, S. P. Ringer, X. S. Zhao, A. T. S. Wee, M. Bosman and Z. Y. Yin, *Nano Energy*, 2023, **115**, 108684.

126 X. Y. Jiang, J. D. Huang, Z. H. Bi, W. J. Ni, G. Gurzadyan, Y. A. Zhu and Z. Y. Zhang, *Adv. Mater.*, 2022, **34**, 202109330.

127 D. Li, C. J. Zhou, X. L. Shi, Q. Zhang, Q. Song, Y. M. Zhou and D. L. Jiang, *Appl. Surf. Sci.*, 2022, **598**, 153843.

128 J. Y. Wang, Y. Z. Li, J. T. Zhao, Z. Xiong, Y. C. Zhao and J. Y. Zhang, *Catal. Sci. Technol.*, 2022, **12**, 3454–3463.

129 Y. Y. Yu, Y. He, P. Yan, S. Y. Wang and F. Dong, *Proc. Natl. Acad. Sci. U. S. A.*, 2023, **120**, 2307320120.

130 B. W. Zhou, Y. J. Ma, P. F. Ou, Z. W. Ye, X. Y. Li, S. Vanka, T. Ma, H. D. Sun, P. Wang, P. Zhou, J. K. Cooper, Y. X. Xiao, I. A. Navid, J. Pan, J. Song and Z. T. Mi, *Nat. Catal.*, 2023, **6**, 987–995.

131 N. Y. Huang, B. Li, D. J. Wu, Z. Y. Chen, B. Shao, D. Chen, Y. T. Zheng, W. J. Wang, C. Z. Yang, M. Gu, L. Li and Q. Xu, *Angew. Chem., Int. Ed.*, 2024, **63**, e202319177.

132 D. W. Zhao, Y. M. Xuan, K. Zhang and X. L. Liu, *ChemSusChem*, 2021, **14**, 3293–3302.

133 W. Lyu, Y. Liu, J. Y. Zhou, D. T. Chen, X. Zhao, R. Q. Fang, F. L. Wang and Y. W. Li, *Angew. Chem., Int. Ed.*, 2023, **62**, 202310733.

134 Y. Zhang, H. L. Shi, S. Y. Zhao, Z. L. Chen, Y. Y. Zheng, G. M. Tu, S. X. Zhong, Y. L. Zhao and S. Bai, *Small*, 2024, **20**, 202304050.

135 Y. X. Miao, Y. X. Zhao, S. Zhang, R. Shi and T. R. Zhang, *Adv. Mater.*, 2022, **34**, 202200868.

136 C. L. Tan, M. Y. Qi, Z. R. Tang and Y. J. Xu, *ACS Catal.*, 2023, **13**, 8317–8329.

137 S. P. Mo, X. Y. Zhao, S. D. Li, L. L. Huang, X. Zhao, Q. M. Ren, M. Y. Zhang, R. S. Peng, Y. A. Zhang, X. B. Zhou, Y. M. Fan, Q. L. Xie, Y. B. Guo, D. Q. Ye and Y. F. Chen, *Angew. Chem., Int. Ed.*, 2023, **62**, 202313868.

138 G. P. Zhang, X. X. Li, D. Y. Chen, N. J. Li, Q. F. Xu, H. Li and J. M. Lu, *Adv. Funct. Mater.*, 2023, **33**, 202308553.

139 R. Z. Chen, S. H. Chen, L. Q. Wang and D. S. Wang, *Adv. Mater.*, 2023, **36**, 202304713.

140 M. Jung, C. W. Kim, S. Y. Kim, A. U. Pawar, D. K. Lee and Y. S. Kang, *Adv. Energy Mater.*, 2022, **12**, 202202160.

141 C. W. Kim, Y. S. Son, M. J. Kang, D. Y. Kim and Y. S. Kang, *Adv. Energy Mater.*, 2016, **6**, 201501754.

142 C. W. Kim, S. J. Yeob, H. M. Cheng and Y. S. Kang, *Energy Environ. Sci.*, 2015, **8**, 3646–3653.

143 A. U. Pawar, C. W. Kim, M. J. Kang and Y. S. Kang, *Nano Energy*, 2016, **20**, 156–167.

144 C. W. Kim, A. U. Pawar, T. Hawari, N. H. Ahn, D. K. Lee, L. Yang, R. P. Sivasankaran, J. Tang, Z. B. Zhuo and Y. S. Kang, *Sci. Rep.*, 2022, **12**, 20045–20046.

145 A. U. Pawar, U. Pal, J. Y. Zheng, C. W. Kim and Y. S. Kang, *Appl. Catal., B*, 2022, **303**, 120921.

146 L. A. Li, Z. C. Chai, W. Jin, H. Sun, J. H. He, G. Q. Wu and W. W. Xia, *J. Alloys Compd.*, 2023, **932**, 167658.